

Modulation-Doping a Correlated Electron Insulator

Debasish Mondal¹, Smruti Rekha Mahapatra¹, Abigail M Derrico², Rajeev Kumar Rai³, Jay R Paudel², Christoph Schlueter⁴, Andrei Gloskovskii⁴, Rajdeep Banerjee¹, Frank M F DeGroot⁵, Dipankar D Sarma¹, Awadhesh Narayan¹, Pavan Nukala³, Alexander X Gray^{2*} and Naga Phani B Aetukuri^{1*}

Affiliations:

1. Solid State and Structural Chemistry Unit, Indian Institute of Science, Bengaluru, Karnataka, 560012, India
2. Department of Physics, Temple University, 1925 N. 12th St., Philadelphia, PA 19122, USA
3. Centre for Nano Science and Engineering, Indian Institute of Science, Bangalore, Karnataka, 560012, India
4. Deutsches Elektronen-Synchrotron, DESY, 22607 Hamburg, Germany
5. Utrecht University, Inorganic Chemistry and Catalysis Group Universiteitsweg 99, 3584 CA Utrecht, The Netherlands

*Corresponding authors emails: phani@iisc.ac.in (N.B.A); axgray@temple.edu (A.X.G)

ABSTRACT

Correlated electron materials (CEMs) host a rich variety of condensed matter phases. Vanadium dioxide (VO₂) is a prototypical CEM with a temperature-dependent metal-to-insulator (MIT) transition with a concomitant crystal symmetry change. External control of MIT in VO₂ – especially without inducing structural changes - has been a long-standing challenge. In this work, we design and synthesize modulation-doped VO₂-based thin film heterostructures that closely emulate a textbook example of filling control in a correlated electron insulator. Using a combination of charge transport, hard x-ray photoelectron spectroscopy, and structural characterization, we show that the insulating state can be doped to achieve carrier densities greater than $5 \times 10^{21} \text{ cm}^{-3}$ without inducing any measurable structural changes. We find that the MIT temperature (T_{MIT}) continuously decreases with increasing carrier concentration. Remarkably, the insulating state is robust even at doping concentrations as high as $\sim 0.2 e^-$ /vanadium. Finally, our work reveals modulation-doping as a viable method for electronic control of phase transitions in correlated electron oxides with the potential for use in future devices based on electric-field controlled phase transitions.

INTRODUCTION

Strong electron-electron correlations within narrow d- or f-orbitals underpin a variety of condensed matter phenomena, such as metal-to-insulator transitions (MITs), high-temperature superconductivity, magnetism, and multiferroicity, often observed in correlated electron materials (CEMs).^{1,2} VO₂ is a prototypical example of a CEM with a temperature-dependent metal-to-insulator phase transition. The electronic phase transition in bulk VO₂, which occurs at a MIT temperature (T_{MIT}) of ~340 K, is accompanied by a structural phase transition from a metallic rutile phase to an insulating monoclinic phase.^{3,4}

The origin of the MIT in VO₂ – whether gap-opening is driven by the symmetry-lowering structural transition or by electron-electron correlations - has been widely studied.⁵⁻⁸ In particular, there is widespread interest in the nature of the insulating state and its external control via doping^{9,10}, strain¹¹, oxygen vacancy creation¹², hydrogenation¹³, light-and-pulse-induced modulation^{14,15}, and via electric-fields in a field-effect transistor geometry^{16,17}.

For example, n-type doping of VO₂ with dopants such as W⁶⁺, Mo⁵⁺, and Nb⁵⁺ was shown to decrease T_{MIT} and stabilize the metallic phase.^{9,10,18} By contrast, p-type doping of VO₂ with dopants such as Cr³⁺, Ga³⁺, and Al³⁺ was shown to increase T_{MIT} , thereby stabilizing the insulating phase.¹⁹⁻²¹ Similarly, both oxygen vacancy creation and hydrogenation were shown to n-dope VO₂ and decrease T_{MIT} .^{12,13,22} Finally, in VO₂ thin films, macroscopic tensile strain along the rutile a-axis was also shown to decrease T_{MIT} .^{11,12}

In all these previous approaches, modulation of T_{MIT} was always associated with macroscopic changes to the lattice parameters (due to strain) and/or dopant-induced local structural distortions.^{9,10,12,13,19,22} In such experiments, where both the lattice strain and carrier concentration change, it is challenging and, sometimes, impossible to disentangle the role of carrier concentration changes from the role of lattice strain. For instance, in the case of W-doped VO₂, an increase in W-doping concentration increases both the carrier density and lattice strain.²³

Other techniques utilizing external stimuli, such as electric-field induced metallization of VO₂ in a field-effect transistor geometry, could, in theory, enable the modulation of its conductivity without inducing macroscopic structural changes. However, previous attempts at electric-field-driven metallization of VO₂ have not been successful.^{12,16,17,24,25} The absence of any

field-effect, even when gated through high-K dielectrics, was attributed to the presence of strong correlations in the insulating VO₂ phase.¹⁶ Further, ionic-liquid gating of VO₂, which could enable accessibility to large interfacial electric-fields, led to oxygen vacancy creation and/or hydrogenation of VO₂.^{12,16}

Modulation- or remote-doping of oxide semiconductors is an alternative method for achieving high dopant carrier densities without inducing local structural distortions.²⁶⁻²⁹ In modulation-doping, a chemical potential mismatch between a high band gap heavily-doped layer (dopant-layer) and a lower band gap undoped layer (channel) leads to charge transfer from the heavily doped dopant-layer to the undoped channel. In general, the dopant layer and the channel are spatially separated by a barrier (or a spacer) layer that kinetically limits the interdiffusion of the dopants from the dopant layer to the channel layer while allowing charge transfer via quantum mechanical tunneling.^{30,31}

Modulation-doping was successfully applied to semiconductors and band-insulating oxides such as ZnO and SrTiO₃.^{27,29,32-35} However, modulation-doping of correlated electron insulators has had limited success. For example, Stemmer and colleagues reported modulation-doping of NdNiO₃, but this did not lead to any significant changes in T_{MIT} of the nickelate.²⁷ Whether modulation-doping could be a generic approach to induce phase transitions in oxides is unclear and several key questions remain unanswered. For example, how do bands evolve in correlated oxides as a function of doping? Can a rigid band model be applied to understand doping in oxides? How sensitive are the ground state properties in correlated oxides to carrier doping?

In this work, we address some of these open questions using the MIT in VO₂ as a model system. We propose a modulation-doped heterostructure to n-dope VO₂ without inducing any structural distortions. Commonly in modulation-doping, an epitaxial structure is grown with a spacer and the dopant layers epitaxially matched to the semiconducting channel layer. Note that both the spacer and dopant layers must be insulating with a bandgap that is higher than that of the channel layer. However, the only stable rutile oxide that is both insulating with a compatible band mismatch that allows modulation doping of VO₂ is TiO₂. The other rutile oxides such as CrO₂, RuO₂, and IrO₂ are metallic and therefore not compatible as dopant layers.^{36,37}

As an additional challenge, oxygen lattice continuity in epitaxial structures might also lead to oxygen vacancy diffusion across the layers.^{22,38,39} We note that oxygen vacancy formation,

which was shown to affect the MIT in VO₂, is commonly observed in transition metal oxides.^{12,40,41} Thus, in order to prevent oxygen vacancy diffusion across the wide band-gap spacer layer as well as to circumvent the lack of lattice-matching insulating rutile oxides, we have gone away from epitaxially-matched modulation-doped heterostructures. Instead, we propose an amorphous LaAlO₃ (LAO) layer (with a reported electronic band gap of ~5.6 eV)⁴² as the spacer layer. Since LAO has a low oxygen vacancy-diffusivity⁴³, we use an amorphous oxygen-deficient TiO_{2-x} as the dopant layer. Stoichiometric TiO₂ has a bandgap of ~3 eV⁴⁴ and TiO_{2-x} is n-type conducting. Using TiO_{2-x} instead of a conventionally doped TiO₂ such as, Nb-doped TiO₂, significantly simplified heterostructure deposition. Furthermore, this approach avoids the interdiffusion of metallic dopants such as Nb in Nb-doped TiO₂ and the associated unintentional doping of VO₂.

The modulation-doped structure for all samples used in this work is comprised of a VO₂ channel layer, a 2 nm thick LAO spacer layer, and a 3 nm thick TiO_{2-x} dopant layer, as shown schematically in Fig. 1a. All heterostructures were capped with a 1 nm thick LAO layer to prevent dopant passivation from atmospheric impurities as well as oxidation of the TiO_{2-x} dopant layer. Fermi level alignment across the structure is expected to lead to an electron accumulation region at the LAO/VO₂ interface. Expected band-alignments for this type-I heterojunction before and after heterostructure formation are shown in Fig. 1b.

To experimentally realize the proposed modulation-doped structure, all samples were grown using pulsed laser deposition (PLD) on single-crystalline TiO₂ (001) substrates. VO₂ was deposited at 425 °C, while all the other amorphous layers were deposited at room temperature (see methods section for details). It is important to note that room-temperature deposition of the spacer, dopant and capping layers also minimizes any interfacial interdiffusion. A cross-sectional scanning transmission electron microscopy (STEM) image (Fig. 1c) and the associated energy dispersive spectroscopy (EDS) elemental maps (Fig. 1d) show abrupt high-quality interfaces between the TiO₂ substrate and the VO₂ film, and between the film and LAO spacer. This data is consistent with in-situ RHEED patterns of the deposited VO₂ films and suggests that the films are both atomically smooth and single-crystalline (SI Fig. S1). The atomic force microscopy (AFM) images of the complete heterostructures further confirm the high quality of the growth by showing atomically smooth film surfaces (SI Fig. S2).

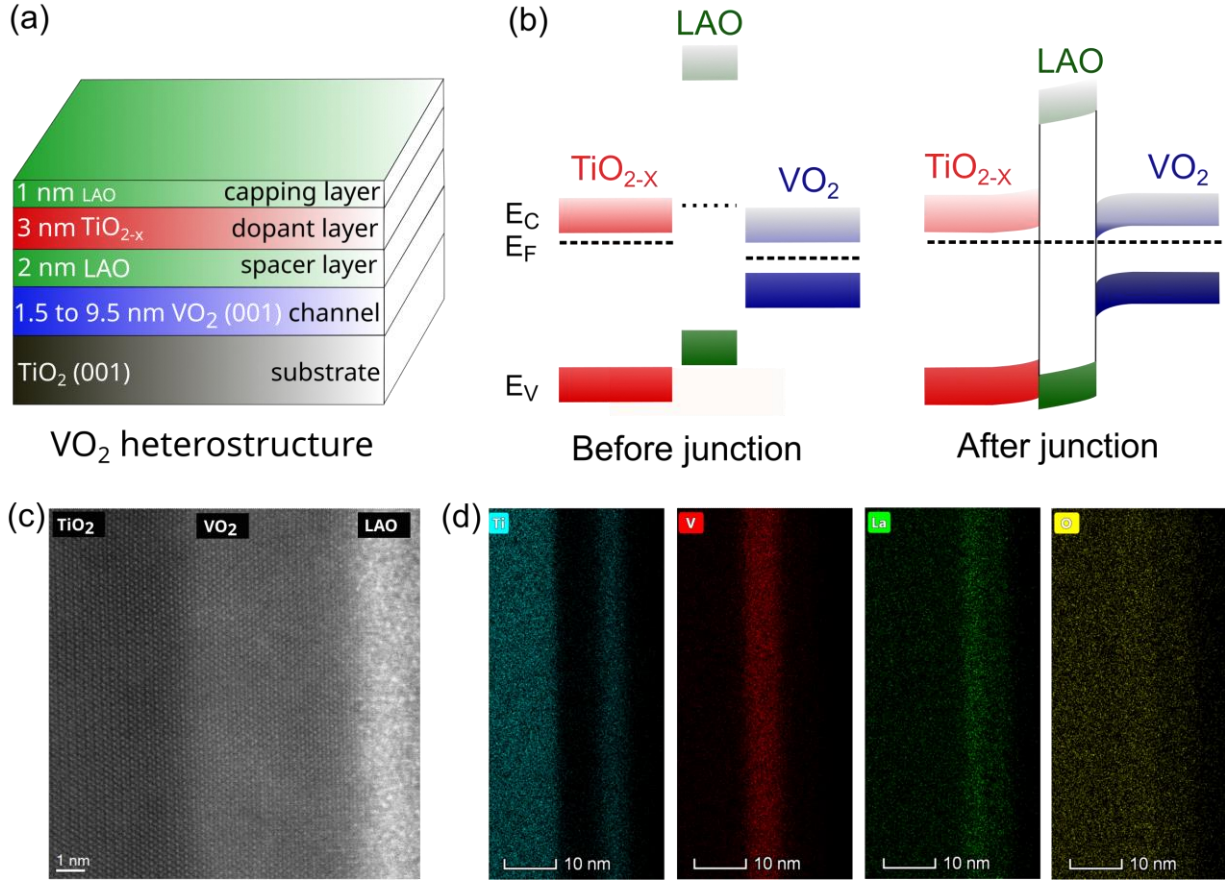


Fig. 1. (a) Schematic diagram of the heterostructures used in this work. The thickness of VO_2 is varied while the thicknesses of all the other layers are as mentioned in the schematic. (b) Schematic energy band diagram for a $\text{VO}_2/\text{LAO}/\text{TiO}_{2-x}$ heterostructure before and after the junction formation. Electron accumulation is expected based on the known band offsets. The color intensities are chosen to be proportional to expected electron densities for better visualization. E_C , E_V , and E_F indicate the conduction band edge, valence band edge, and Fermi level, respectively. (c) High-resolution cross-sectional high-angle annular dark-field scanning transmission electron microscopy (HAADF-STEM) image showing abrupt interfaces between TiO_2 substrate and VO_2 film and VO_2 film and the amorphous LAO spacer layer. (d) Elemental mapping using energy dispersive x-ray spectroscopy (EDS) showing the various layers in the heterostructure. Note that the scales of (c) and (d) are different.

To study the correlation between modulation-doping-induced carrier density changes and the changes in the MIT characteristics, we deposited several modulation-doped heterostructures with varying thicknesses of the VO_2 layer ranging from 1.5 nm to 9.5 nm, while keeping the thickness of the TiO_{2-x} layer unchanged at 3 nm. Thomas-Fermi screening lengths in VO_2 are expected to be on the order of 1 nm (SI section S3) and, therefore, the highest n-type carrier densities are expected for the lowest VO_2 film thickness used in this study (~1.5 nm).

Heterostructures with VO₂ films thinner than ~1.5 nm were not attempted due to the expected titanium interdiffusion at the VO₂ film and TiO₂ substrate interface.^{45,46} We note that interfacial titanium interdiffusion will be present in thicker films as well. However, at VO₂ thicknesses greater than 1.5 nm, there is still an observable MIT.

A summary of the θ -2 θ X-ray diffraction (XRD) measurements, performed at room temperature, for a 9.5 nm VO₂ film and the VO₂/LAO/TiO_{2-x}/LAO heterostructures on TiO₂(001) substrates are shown in Fig. 2a. Clearly, the angular positions of the VO₂ (002) Bragg reflection peaks are identical for both the 9.5 nm VO₂ film (purple spectrum) and the 9.5 nm VO₂ heterostructure (blue spectrum). Furthermore, it is evident that the angular position of the Bragg reflection is essentially independent of the thickness of the VO₂ film in the heterostructure. Additionally, there were no significant changes in the θ -2 θ X-ray diffractograms between VO₂ films and heterostructures with the same VO₂ thickness (SI Fig. S4). Reciprocal space maps also confirm that all samples are coherently strained in the plane of the TiO₂(001) substrate. The out-of-plane rutile c-axis lattice parameter is identical for the thin film and the heterostructures for all thicknesses of VO₂ (SI Fig. S5). Based on the θ -2 θ XRD measurements, reciprocal space maps, and cross-sectional STEM imaging we conclude that the lattice parameter changes, if any, are within the instrumental resolution (better than 0.1 pm) for all the VO₂ heterostructures used in this work. We also note that the reflections for the LAO spacer and capping layers and the TiO_{2-x} dopant layer are absent, suggesting that these layers are not crystalline.

Next, we discuss the variations in the MIT characteristics for the same set of samples as used in the XRD studies. As shown in Fig. 2b, T_{MIT} systematically decreases with decreasing VO₂ thickness in the heterostructure. Note that the decrease in T_{MIT} for thin films of VO₂ is thickness independent (SI Fig. S6), suggesting that the decrease in T_{MIT} for VO₂ heterostructures is intrinsic to heterostructure formation. Furthermore, the sheet resistance of VO₂ heterostructures in the insulating state also decreases (SI Fig. S7). Except for the heterostructure with the thinnest VO₂ layer (1.5nm), all films continue to show a positive temperature coefficient of resistance, suggesting metallicity above T_{MIT}.

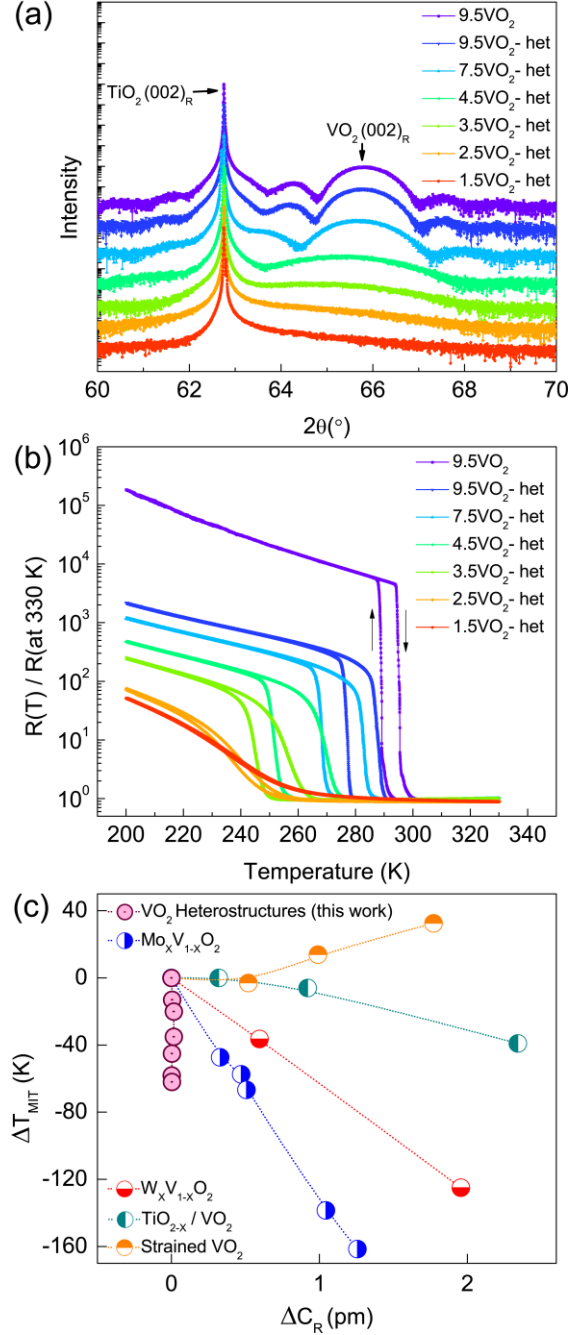


Fig. 2. (a) High-resolution θ - 2θ XRD spectra for the 9.5 nm VO_2 thin film and for VO_2 heterostructures with varying thicknesses, t . For nomenclature simplicity, we distinguish VO_2 thin films and heterostructures with a VO_2 thickness of ‘ t ’ as $t\text{VO}_2$ and $t\text{VO}_2\text{-het}$, respectively. For example, $9.5\text{VO}_2\text{-het}$ corresponds to a heterostructure with 9.5 nm thick VO_2 . (b) Resistance versus temperature plots for the same set of samples as shown in (a). Resistance values presented here are normalized to the resistance at 330 K and were measured in Van der Pauw geometry (also see SI Fig. S3). Clearly, T_{MIT} decreases with decreasing VO_2 thickness in the heterostructure. (c) A comparison of the changes in T_{MIT} versus the changes in the rutile C-axis lattice parameter (ΔT_{MIT} vs ΔC_R) for this work and other previously published work using W^9 - and Mo^{10} -doping (red and blue respectively), oxygen vacancy doping²² (gray) and strain¹¹ (orange). The relative changes are compared to the undoped and unstrained states in the case of bulk doping and for strained VO_2 . For the modulation-doped heterostructures, the reference state is taken as a 9.5 nm VO_2 thin film on $\text{TiO}_2(001)$ substrate.

We summarize our observations and compare the changes in T_{MIT} with other previously published studies in Fig. 2c (also see SI Fig. S8 for details regarding T_{MIT} calculation). Significantly, there is a nearly 60 K change in T_{MIT} for the thinnest heterostructures without any measurable changes to the rutile C-axis. In contrast, any comparable change in T_{MIT} in the literature is associated with ΔC_R greater than 0.5 pm. This demonstrates control over the MIT in VO_2 without any measurable structural changes in the VO_2 heterostructures proposed and synthesized in this work. We note that a decrease in T_{MIT} was observed for elemental doping of VO_2 with n-type dopants such as W and Mo, while an increase in T_{MIT} was observed for hole-doping with elements such as Cr and Al. There is no W or Mo in any of the heterostructures in this work, and both La and/or Al doping can be ruled out because they would (if anything) lead to hole-doping resulting in an increase in the T_{MIT} . This is contrary to the decrease in T_{MIT} observed in these VO_2 heterostructures.

To measure the extent and type of doping, we performed temperature-dependent Hall measurements. Hall measurements show an enhancement in the carrier densities in the insulating state with the Hall coefficient indicative of electron-doping (Fig. 3a). On the other hand, carrier densities in the insulating phase increased from $\sim 6 \times 10^{17} \text{ cm}^{-3}$ (for 9.5 nm VO_2 thin film) to $\sim 2.8 \times 10^{19} \text{ cm}^{-3}$ (for 9.5 nm VO_2 heterostructure) to a highest of $\sim 5 \times 10^{21} \text{ cm}^{-3}$ for the 2.5 nm VO_2 heterostructure. Contrastingly, the metallic state carrier densities remain identical ($\sim 6 \times 10^{22} \text{ cm}^{-3}$) across all the VO_2 heterostructures and are consistent with previous reports.^{12,24}

However, carrier mobility decreases in both the insulating and metallic states as the thickness of the VO_2 layer decreases (Fig. 3b). In the metallic state, this is potentially due to contributions from interfacial scattering, which increases with decreasing film thickness. In the insulating state, the decrease in carrier mobility could result in part from increased electron-electron scattering and interfacial scattering. A summary of the changes in carrier concentration is plotted against T_{MIT} in Fig. 3c. There is a clear correlation between the T_{MIT} and the carrier density with the highest carrier density of $\sim 5 \times 10^{21} \text{ cm}^{-3}$ stabilizing the metallic state of VO_2 to a T_{MIT} of $\sim 237 \text{ K}$ (SI Fig. S8). Importantly, the continuous increase in carrier density with decreasing VO_2 thickness without any lattice parameter changes is suggestive of modulation-doping in VO_2 heterostructures.

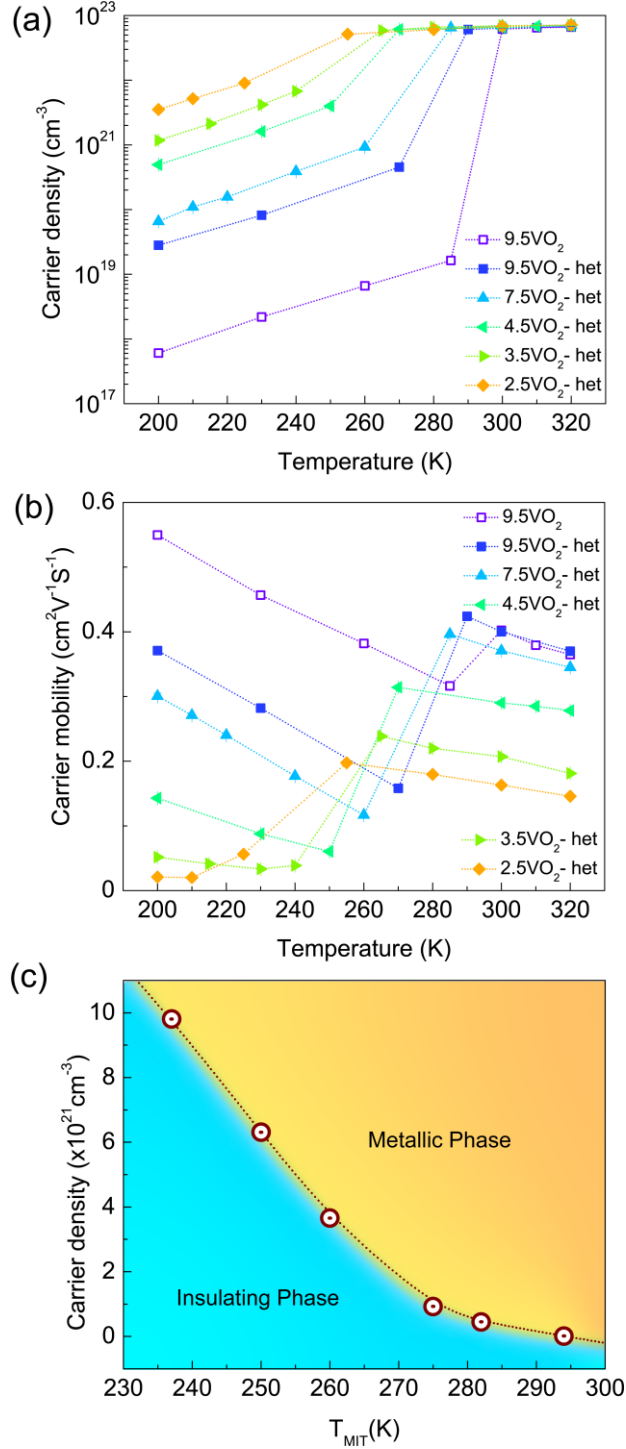


Fig. 3. Plots of temperature-dependent (a) carrier densities and (b) carrier mobilities for *t*VO₂ and *t*VO₂-het samples as mentioned in the legends. Carrier density in the insulating state increases with decreasing VO₂ thickness while carrier mobility decreases. (c) A phase diagram from the results in (a). The dotted lines connected across the data points are guide to the eye.

To further establish that most of the carriers are induced by modulation doping, we prepared two additional control samples. The first is a 7.5 nm VO₂ thin film with a 2 nm LAO cap layer (7.5VO₂-LAO) and the second is a 7.5 nm VO₂ heterostructure with a 3 nm stoichiometric TiO₂ layer (7.5VO₂-LAO-TiO₂). We compared the MIT characteristics of these two samples with the MIT characteristics of the 7.5 nm VO₂ thin film (7.5VO₂) and a 7.5 nm VO₂ heterostructure with a TiO_{2-x} dopant layer (7.5VO₂-het). A summary of sheet resistance versus temperature data is shown in SI Fig. S9. The 7.5 nm VO₂ heterostructure with a TiO_{2-x} dopant layer has the lowest sheet resistance and the lowest T_{MIT} with a T_{MIT} change of ~20 K. By contrast, the decrease in T_{MIT} was restricted to ~6 K after the deposition of the 2 nm LAO layer. Remarkably, there is no further decrease in T_{MIT} in the heterostructure with stoichiometric TiO₂ layer, suggesting that the TiO_{2-x} dopant layer is required for the observed large change in T_{MIT}.

Consistent with this, the carrier density in the 7.5 nm VO₂ heterostructure with the TiO_{2-x} dopant layer is ~7x10¹⁹ cm⁻³ compared to a carrier density of 2x10¹⁹ cm⁻³ for the 7.5 nm VO₂ capped with 2 nm LAO (SI Fig. S10). It is possible that amorphous (disordered) LAO could host ionized donors and enable modulation-doping.²⁹ However, we found that the amorphous LAO deposited for these experiments is insulating, suggesting that any ionized donors should be below the measurement threshold of electrical resistivity measurements. We estimate that such ionized donors in LAO, if any, should have a carrier density of ~10¹⁹ cm⁻³ (assuming a carrier mobility of 0.01 cm²/V-s) or lower, putting an upper bound on the number of carriers contributed by the spacer layer.

To probe the electronic band bending that enables electron accumulation in the VO₂ channel layer, we performed bulk-sensitive hard X-ray photoelectron spectroscopy (HAXPES)⁴⁷ measurements at the P22 beamline in the PETRA III synchrotron at DESY. We note that standard ultra-violet photoemission (UPS) or soft X-ray photoemission measurements cannot facilitate a probing depth sufficient to reach the VO₂/LAO interface that is buried beneath multiple layers of the heterostructure. To capture interfacial band bending in VO₂, HAXPES measurements were performed in both the insulating phase (at 200 K) and the metallic phase (at 310 K) for VO₂ heterostructures with VO₂ thicknesses of 1.5 nm, 3.5 nm, 4.5 nm, and 7.5 nm, and for a VO₂ thin film with a thickness of 7.5 nm as a reference.

For the 7.5 nm VO₂ film measured at 200 K (insulating state), the binding energies of the V 2p_{3/2} and V 2p_{1/2} core-level peaks were observed to be ~515.8 eV and ~523.1 eV, respectively (see Fig. 4a). These measured binding energies (see SI Fig. S11 for binding energy calibration procedure) are consistent with previous reports.^{48–50} Importantly, a systematic shift of the main component of the V 2p_{3/2} peak to higher binding energies is observed for the VO₂ heterostructures, with the highest increase in binding energy (~250 meV) observed for the heterostructure with the thinnest VO₂ layer (1.5 nm), as seen in the inset. This is also in agreement with the highest carrier densities and the lowest T_{MIT} being observed for the heterostructures with the thinnest VO₂ layers. For measurements performed on VO₂ in the metallic state, no such binding energy shift was observed (Fig. 4b and SI Fig. S12). This is consistent with the complete screening of interfacial electric fields at the metallic VO₂/LAO interface (Figs. 4c and d). The presence of binding energy shifts observed in the insulating state of VO₂ and their absence in the metallic state of VO₂ further support carrier doping by chemical potential shifts (modulation-doping) in the insulating state for VO₂ heterostructures as proposed in this work.

Photoemission data also showed two remarkable features in the V 2p spectra. The first, labelled *PI* in Figs. 4a and 4b, is a lower binding energy shoulder around ~514.5 eV in the insulating and metallic states. The presence of this spectral feature at lower binding energies was proposed to signify non-local screening from coherent 3d¹ states near E_F in the metallic phase of VO₂.^{50,51} Interestingly, the intensity of *PI* in the insulating state increases with increasing carrier density and decreasing VO₂ thickness in the heterostructures. The emergence of this peak in the insulating state spectra for VO₂ heterostructures suggests that the additional charge transferred to the VO₂ channel layer enables non-local screening that was previously observed only in the metallic phase of VO₂.

To further quantify the evolution of the *PI* peak across the metallic and insulating phases, we compared the metallic and insulating state spectra of 1.5 nm and 7.5 nm VO₂ heterostructures in SI Fig. S13. The intensity of the *PI* peak in the insulating state of the 7.5 nm VO₂ heterostructure is observable but small in comparison to the *PI* peak in the metallic state (SI Fig. S13a). The difference spectrum shows a large difference at ~514.5 eV (SI Fig. S13c) further confirming that the non-locally screened shoulder is negligibly small in the insulating state when compared to the metallic state. Remarkably, the non-locally screened shoulder is quite predominant in the

insulating state spectra of 1.5 nm VO₂ heterostructure (SI Fig. S13b). The intensity difference spectra between the metallic and insulating states shows a very small difference between the two phases (Fig. S13d). These trends are consistent with the differences in the carrier densities between the metallic and insulating phases. The carrier density ratio between the metallic and insulating states is about 10 for the 1.5 nm VO₂ heterostructure compared to about 1000 for the 7.5 nm VO₂ heterostructure.

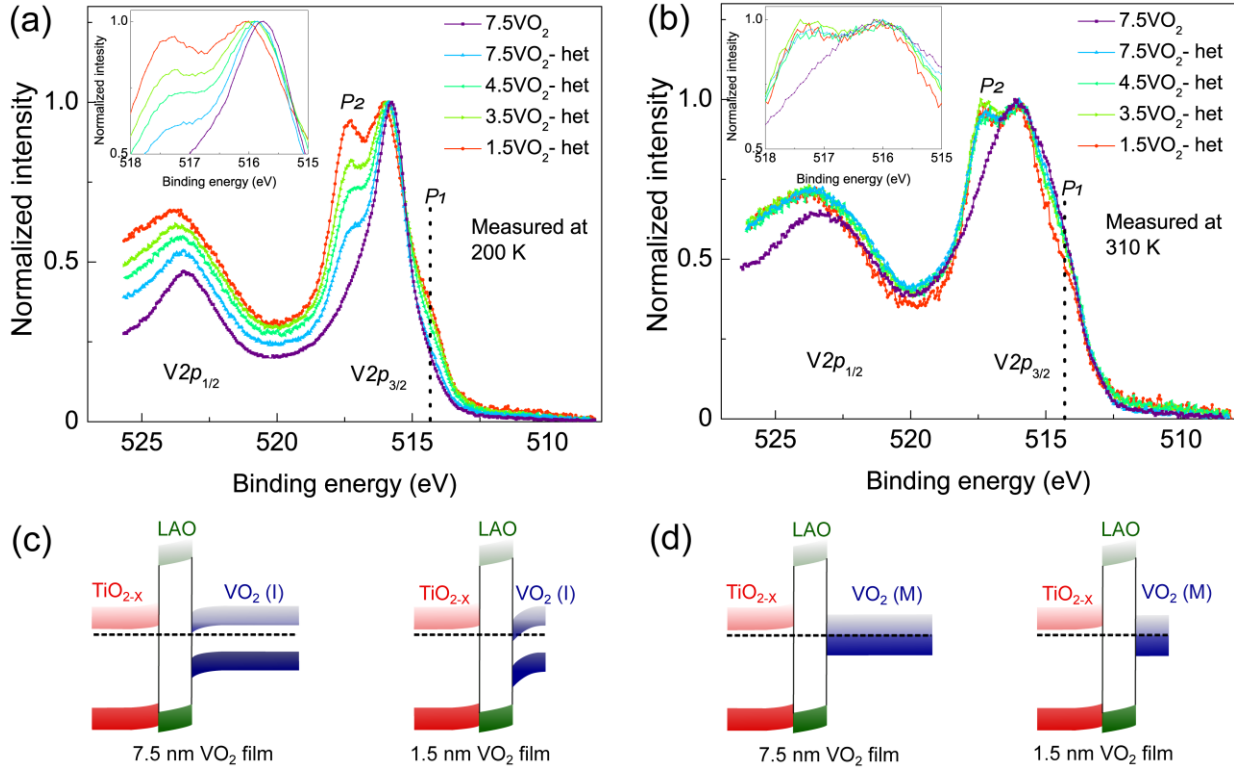


Fig. 4. A comparison of V 2p core-level spectra of modulation doped VO₂ heterostructures for (a) the insulating (200 K) and (b) the metallic states (at 310 K). A clear shift in the V 2p levels is seen in the insulating state spectra but not in the metallic state spectra. Schematics in (c) and (d) show the expected band-bending in the modulation-doped heterostructures for the insulating and metallic states respectively. Band-bending is expected in the insulating state and not in the metallic state. Two additional spectral features not seen in VO₂ thin films are labelled P1 and P2.

The second remarkable feature in the photoemission data is a high binding energy spectral feature at ~517.5 eV. This feature is associated with the V 2p_{3/2} peak and labelled P2 in Figs. 4a and b. A corresponding feature is also observed for the V 2p_{1/2} peak but is more smeared out and appears as broadening on the higher-binding-energy side at ~525 eV. In general, higher binding energy spectral features are associated with higher oxidation states in photoemission. The presence

of V^{5+} is a possibility. However, an increase in the oxidation state from V^{4+} to V^{5+} cannot explain the observed electron-doping in VO_2 heterostructures. Generally, electron doping should decrease the V^{4+} oxidation state in VO_2 and therefore, an increase in the oxidation state of vanadium cannot explain the increase in electron density in the VO_2 heterostructures. Therefore, V^{5+} , even if present, has no bearing on the MIT observed in heterostructures.

$P2$ was also observed in VO_2 samples capped with 2 nm LAO (SI Fig. S14). Therefore, we have also inspected the La $3d_{5/2}$ and Al $1s$ spectra to look for any chemical shifts associated with a redox or chemical reaction at the VO_2 /LAO interface. As shown in SI Fig. S15, there are no observable changes to the spectra across heterostructures. Finally, interfacial oxygen vacancy creation remains a possibility. However, any oxygen vacancy creation should lead to V^{3+} and an associated low-binding-energy feature in both the metallic and insulating state spectra. However, the spectra do not show any signatures of oxygen vacancies in VO_2 heterostructures. Therefore, we rule out any oxygen-vacancy induced carrier doping in these heterostructures.

Furthermore, the intensity of $P2$ is carrier density dependent. For all V $2p$ spectra in the metallic state, where the carrier density is independent of the VO_2 thickness, the intensity of this additional peak relative to the main V $2p_{3/2}$ peak is also independent of the VO_2 thickness, with the intensity ratio of $P2$ to V $2p_{3/2}$ being close to 1. Contrastingly, the intensity of $P2$ increases with the decreasing film thickness in the insulating state of VO_2 . The intensity ratio of $P2$ to V $2p_{3/2}$ approaches the intensity ratio observed for the metallic state spectra at the highest carrier density of $\sim 5 \times 10^{21} \text{ cm}^{-3}$ in the insulating state. These carrier-density-dependent changes suggest that this new spectral feature is intrinsic to the heterostructure. However, this additional spectral feature might benefit from further spectroscopic investigation with complementary techniques such as X-ray absorption spectroscopy to confirm its origins.

The combination of electron transport and HAXPES data show that VO_2 heterostructures facilitated effective modulation doping and carrier densities as high as $5 \times 10^{21} \text{ cm}^{-3}$ could be achieved using this approach. The highest carrier densities correspond to electron doping of ~ 0.2 e-/vanadium. This is an extremely high dopant density at which conventional rigid band models predict metallization in doped correlated insulators.⁵²

Bulk-sensitive valence-band HAXPES spectra recorded for the same set of heterostructures as discussed in Fig. 4 are shown in Fig. 5 and SI Fig. S16. The insulating-state spectra for all VO_2

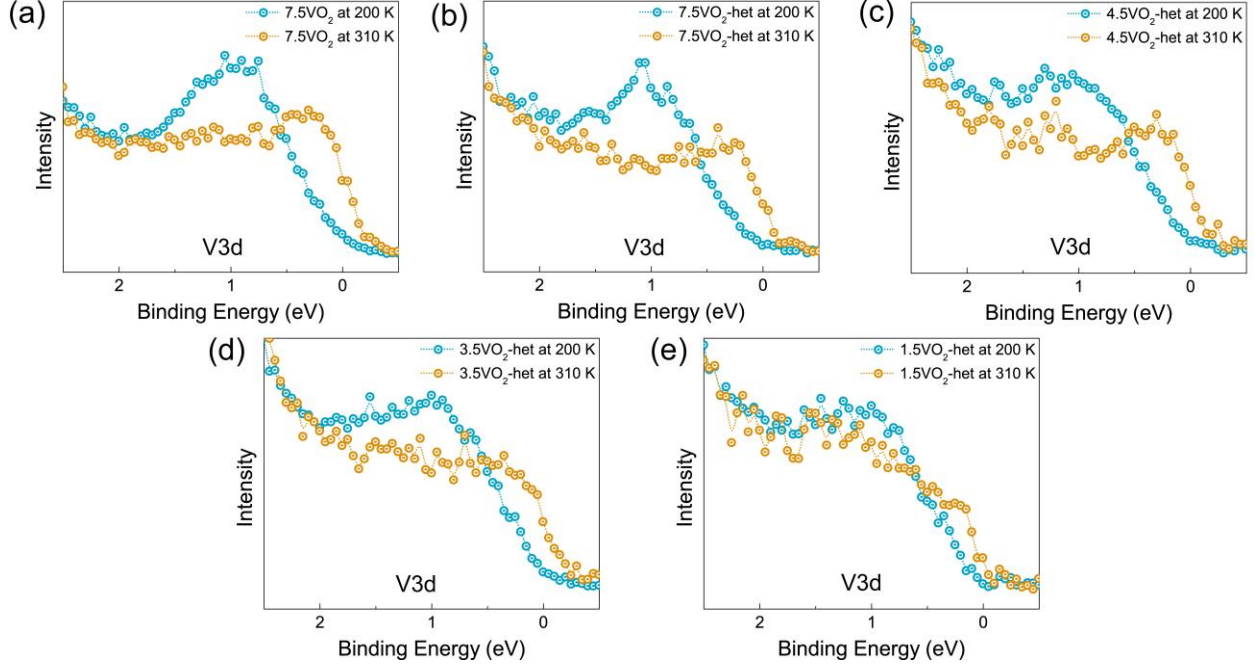


Fig. 5. A comparison of the V 3d valence band (VB) spectra of modulation-doped VO_2 heterostructures for the insulating (200 K, blue) and metallic states (at 310 K, orange) for different VO_2 film thicknesses of (a) 7.5 nm VO_2 film and (b) 7.5 nm, (c) 4.5 nm, (d) 3.5 nm, and (e) 1.5 nm VO_2 heterostructures. There is a clear spectral weight shift across the MIT for all the samples with the insulating state being robust even for the heterostructure with a VO_2 thickness of 1.5 nm, corresponding to carrier doping of ~ 0.2 e-/Vanadium.

heterostructures (blue) exhibit nearly zero spectral intensity at the Fermi level while an appreciable non-zero spectral intensity is observed for the higher-temperature metallic-state spectra (orange). These spectra further confirm that VO_2 continues to undergo a MIT even in the presence of electron densities as high as ~ 0.2 e-/vanadium. The presence of MIT at such high doping levels, without any observable changes in the lattice parameters (Fig. 2a and SI Fig. S4), points to a possible renormalization of the electronic structure with doping.

Conclusions:

In summary, we demonstrated a purely electronic control of the MIT in modulation-doped VO_2 heterostructures. Our work shows that the insulating state in VO_2 is surprisingly robust even in the presence of electron doping as high as 0.2 e-/vanadium. Notably, all the films meet the Mott criterion ($a_B \cdot n_C^{\frac{1}{3}} > 0.25$, where a_B is the effective Bohr radius and n_C is the carrier density). Therefore, metallicity is expected at all temperatures based on the carrier densities achieved in these experiments. We note that a similar robust insulating state had also been found in

modulation-doped nickelate thin films.²⁷ Perhaps, the development of theoretical models that go beyond the conventional carrier concentration independent rigid-band models will be required to understand electronic phase transitions in correlated electron oxides. An alternate explanation could be that the insulating state is favored at lower thicknesses due to interfacial disorder-induced Anderson-like localization of carriers, which will be more pronounced for the thinnest films. Further experiments will be needed to assess whether the insulating state is stabilized by the interfacial disorder.

A remarkable feature of this work is the possibility of bulk metallization in modulation-doped VO₂. In general, in band semiconductors such as SrTiO₃, conductivity modulation is achieved over a thickness of 1-2 nm in the vicinity of the channel/spacer interface.^{29,53} In this work, a sharp MIT is observed for heterostructures with VO₂ thicknesses as high as 9.5 nm, which are much higher than the Thomas Fermi screening length of ~1 nm. This is suggestive of the entirety of the film being metallized at the lowered T_{MIT} after modulation doping, even though the charge transfer densities are the highest at the interface (within 1-2 nm of the interface). While further studies are required to establish this beyond doubt, interfacial-doping induced bulk metallization of correlated electron insulators has implications for low-power electronics with high ON/OFF ratios.^{28,54}

Finally, our work shows that modulation doping is a powerful technique for achieving high carrier densities, close to those possible with elemental doping. Since our approach does not need any epitaxially matched spacer and dopant layers, it expands the library of materials that can be explored for the study of modulation-doping-induced electronic phase transitions of other related CEMs including complex oxides² and pyrochlores⁵⁵. This methodology, therefore, paves the way for exploring ‘pure’ electronic effects in correlated oxides and related systems. Such studies could also enable a fundamental understanding of band matching and relevant energy scales in complex oxides and, perhaps enable the discovery of new interfacial phases and devices that rely on phase transitions.

Methods

Prior to deposition, single-crystalline rutile TiO₂ (001) substrates (Shinkosa, Japan) were treated using the procedure discussed previously.⁵⁶ All thin film samples were deposited using PLD (NEOCERA) with a 248 nm KrF laser. All VO₂ thin films (both pristine films and

heterostructures) were deposited on treated TiO₂ substrates from a sintered V₂O₅ target with a laser fluence of $\sim 1.5 \text{ J/cm}^2$, 8 mTorr of oxygen pressure, and a growth rate of $\sim 4.7 \times 10^{-2} \text{ \AA/pulse}$ at a substrate temperature of 425 °C.⁵⁶ For all heterostructure samples, 2 nm thick LAO spacer layers were deposited at 10 mTorr of O₂ pressure at a growth rate of $\sim 5 \times 10^{-2} \text{ \AA/pulse}$ using a single-crystalline LAO target (Shinkosa Japan). 3 nm thick TiO_{2-x} dopant layers were then deposited using a TiO_{2-x} single-crystalline target (Shinkosa Japan) at a growth rate of $\sim 4.2 \times 10^{-2} \text{ \AA/pulse}$ in 10⁻⁵ Torr of background vacuum. Finally, a 1 nm thick LAO layer was deposited under the same conditions used for the LAO spacer layer. Depositions of the spacer, dopant, and capping layers were all done at room temperature at a laser fluence of $\sim 1.2 \text{ J/cm}^2$. For all depositions, the substrate-to-target distance was maintained at 55 mm.

High-resolution Cu-K α X-ray diffraction spectra for both the pristine and heterostructure VO₂ films were recorded in standard θ - 2θ geometry using a Rigaku Smart Lab X-ray diffractometer. LEPTOS 7.8 software by Bruker was used to determine film thicknesses and used to calculate the differential strain between pristine and heterostructure films.

Cross-sectional scanning transmission electron microscopy (STEM) imaging and electron dispersive x-ray spectroscopy (EDS) mapping were performed using TITAN Themis microscope (60-300 kV) equipped with a probe corrector and super-X four quadrant EDS detector. The high angle annular dark field (HAADF)-STEM images were acquired at an operating potential of 300 kV with a convergence angle of 24.5 mrad, 160 mm camera length, and a dwell time of 12 μs per pixel. The images were further processed with Gatan digital micrograph software. The EDS maps were acquired using Velox software under similar microscopic conditions with a dwell time of 2 μs per pixel.

Sheet resistance vs temperature measurements were performed in Van der Pauw geometry using Keithley 2450 SMU and Eurotherm 2408 PID temperature controller. Continuous temperature scanning was carried out at a rate of 4 K/minute for both heating and cooling cycles.

To extract carrier density and mobility, Hall measurements for all films and heterostructures were performed using Van der Pauw geometry in a PPMS-Dynacool equipment from Quantum Design and Keithley SMU 2450 from Tektronix. For these measurements, the magnetic field was swept from 0 T to 2 T to -2 T to 0 T at a scan rate of 100 Oe/s for different temperatures ranging from 200 K to 320 K.

High-resolution hard X-ray photoelectron spectroscopy (HAXPES) measurements⁵⁷ were carried out with an incident photon energy of 6.2 keV at the sample temperatures of 200 K (insulating phase) and 310 K (metallic phase). Binding energy calibration was carried out using a high-resolution Fermi-edge measurement on a standard Au sample. Core-level and valence-band spectra were measured using a wide acceptance angle SPECS Phoibos 225HV hemispherical electrostatic analyzer in a near-normal emission geometry. The total energy resolution was estimated to be approximately 320 meV. Preliminary HAXPES measurements and sample screening were carried out using a lab-based HAXPES instrument at Temple University equipped with a wide acceptance angle ScientaOmicron EW4000 analyzer at a total experimental energy resolution of 450 meV.

Acknowledgments:

AXG, AMD, and JRP acknowledge support from the DOE, Office of Science, Office of Basic Energy Sciences, Materials Sciences, and Engineering Division under Award No. DE-SC0019297. The electrostatic photoelectron analyzer for the lab-based HAXPES measurements at Temple University was acquired through an Army Research Office DURIP grant (Grant No. W911NF-18-1-0251). We acknowledge DESY (Hamburg, Germany), a member of the Helmholtz Association HGF, for the provision of experimental facilities. Beamtime at DESY was allocated for proposal I-20210142. Funding for the HAXPES instrument at beamline P22 by the Federal Ministry of Education and Research (BMBF) under framework program ErUM is gratefully acknowledged. PN and RKR acknowledge the Advanced Facility for Microscopy and Microanalysis (AFMM) for providing the electron microscope and FIB facility. A.N. acknowledges support from the startup grant at Indian Institute of Science (SG/MHRD-19-0001). The authors acknowledge CeNSE, IISc for access to HR-XRD, wire bonding, and clean-room facilities. N.B.A. acknowledges the new faculty startup grant provided by the Indian Institute of Science under Grant No. 12-0205-0618-77. N.B.A. is thankful to Professor Anil Kumar for access to the PLD system. S.R.M. and D.M. want to thank Jibin J. Samuel and Mithun Ghosh for useful discussions. We thank Professor Satish Patil for providing access to facilities supported by the Swarnajayanti fellowship under Grant No. DST/SJF/CSA-01/2013-14. AFM measurements were performed on a Cypher-ES AFM funded by the DST-FIST program and Hall measurements were performed on a PPMS-Dynacool system funded under the UGC-CAS program.

References:

1. Dagotto, E. & Tokura, Y. Strongly Correlated Electronic Materials: Present and Future. *MRS Bulletin* **33**, 1037–1045 (2008).
2. Imada, M., Fujimori, A. & Tokura, Y. Metal-insulator transitions. *Rev. Mod. Phys.* **70**, 1039–1263 (1998).
3. Morin, F. J. Oxides Which Show a Metal-to-Insulator Transition at the Neel Temperature. *Phys. Rev. Lett.* **3**, 34–36 (1959).
4. Goodenough, J. B. The two components of the crystallographic transition in VO₂. *Journal of Solid State Chemistry* **3**, 490–500 (1971).
5. Wentzcovitch, R. M., Schulz, W. W. & Allen, P. B. VO₂: Peierls or Mott-Hubbard? A view from band theory. *Phys. Rev. Lett.* **72**, 3389–3392 (1994).
6. Zylbersztein, A. & Mott, N. F. Metal-insulator transition in vanadium dioxide. *Phys. Rev. B* **11**, 4383–4395 (1975).
7. Biermann, S., Poteryaev, A., Lichtenstein, A. I. & Georges, A. Dynamical Singlets and Correlation-Assisted Peierls Transition in VO₂. *Phys. Rev. Lett.* **94**, 026404 (2005).
8. Gray, A. X. *et al.* Correlation-Driven Insulator-Metal Transition in Near-Ideal Vanadium Dioxide Films. *Phys. Rev. Lett.* **116**, 116403 (2016).
9. Shibuya, K., Kawasaki, M. & Tokura, Y. Metal-insulator transition in epitaxial V_{1-x}W_xO₂ (0 ≤ x ≤ 0.33) thin films. *Appl. Phys. Lett.* **96**, 022102 (2010).
10. Holman, K. L. *et al.* Insulator to correlated metal transition in V_{1-x}Mo_xO₂. *Phys. Rev. B* **79**, 245114 (2009).
11. Aetukuri, N. B. *et al.* Control of the metal–insulator transition in vanadium dioxide by modifying orbital occupancy. *Nature Phys* **9**, 661–666 (2013).
12. Jeong, J. *et al.* Suppression of Metal-Insulator Transition in VO₂ by Electric Field–Induced Oxygen Vacancy Formation. *Science* **339**, 1402–1405 (2013).
13. Wei, J., Ji, H., Guo, W., Nevidomskyy, A. H. & Natelson, D. Hydrogen stabilization of metallic vanadium dioxide in single-crystal nanobeams. *Nature Nanotech* **7**, 357–362 (2012).
14. Cavalleri, A., Dekorsy, Th., Chong, H. H. W., Kieffer, J. C. & Schoenlein, R. W. Evidence for a structurally-driven insulator-to-metal transition in VO₂: A view from the ultrafast timescale. *Phys. Rev. B* **70**, 161102 (2004).

15. Liu, M. *et al.* Terahertz-field-induced insulator-to-metal transition in vanadium dioxide metamaterial. *Nature* **487**, 345–348 (2012).
16. Martens, K. *et al.* Field Effect and Strongly Localized Carriers in the Metal-Insulator Transition Material VO₂. *Phys. Rev. Lett.* **115**, 196401 (2015).
17. Sengupta, S. *et al.* Field-effect modulation of conductance in VO₂ nanobeam transistors with HfO₂ as the gate dielectric. *Appl. Phys. Lett.* **99**, 062114 (2011).
18. Piccirillo, C., Binions, R. & Parkin, I. P. Nb-Doped VO₂ Thin Films Prepared by Aerosol-Assisted Chemical Vapour Deposition. *European Journal of Inorganic Chemistry* **2007**, 4050–4055 (2007).
19. Marezio, M., McWhan, D. B., Remeika, J. P. & Dernier, P. D. Structural Aspects of the Metal-Insulator Transitions in Cr-Doped VO₂. *Phys. Rev. B* **5**, 2541–2551 (1972).
20. Pintchovski, F., Glaunsinger, W. S. & Navrotsky, A. Experimental study of the electronic and lattice contributions to the VO₂ transition. *Journal of Physics and Chemistry of Solids* **39**, 941–949 (1978).
21. Brückner, W., Gerlach, U. & Thuss, B. Phase Diagram of V_{1-x}Al_xO₂. *physica status solidi (a)* **40**, K131–K134 (1977).
22. Park, Y. *et al.* Directional ionic transport across the oxide interface enables low-temperature epitaxy of rutile TiO₂. *Nat Commun* **11**, 1401 (2020).
23. Takami, H., Kanki, T., Ueda, S., Kobayashi, K. & Tanaka, H. Filling-controlled Mott transition in W-doped VO₂. *Phys. Rev. B* **85**, 205111 (2012).
24. Nakano, M. *et al.* Collective bulk carrier delocalization driven by electrostatic surface charge accumulation. *Nature* **487**, 459–462 (2012).
25. Ji, H., Wei, J. & Natelson, D. Modulation of the Electrical Properties of VO₂ Nanobeams Using an Ionic Liquid as a Gating Medium. *Nano Lett.* **12**, 2988–2992 (2012).
26. Lee, W.-C. & MacDonald, A. H. Modulation doping near Mott-insulator heterojunctions. *Phys. Rev. B* **74**, 075106 (2006).
27. Son, J. *et al.* Probing the metal-insulator transition of NdNiO₃ by electrostatic doping. *Appl. Phys. Lett.* **99**, 192107 (2011).
28. Son, J., Rajan, S., Stemmer, S. & James Allen, S. A heterojunction modulation-doped Mott transistor. *Journal of Applied Physics* **110**, 084503 (2011).

29. Chen, Y. Z. *et al.* Extreme mobility enhancement of two-dimensional electron gases at oxide interfaces by charge-transfer-induced modulation doping. *Nature Mater* **14**, 801–806 (2015).
30. Dingle, R., Störmer, H. L., Gossard, A. C. & Wiegmann, W. Electron mobilities in modulation-doped semiconductor heterojunction superlattices. *Appl. Phys. Lett.* **33**, 665–667 (1978).
31. Sze, S. M. *Semiconductor Devices: Physics and Technology, 2nd Edition.* (John Wiley & Sons, 2008).
32. Koike, K. *et al.* Molecular Beam Epitaxial Growth of Al-doped ZnMgO Alloy Films for Modulation-doped ZnO/ZnMgO Heterostructures. *Jpn. J. Appl. Phys.* **44**, 3822 (2005).
33. Khim, D. *et al.* Modulation-Doped In₂O₃/ZnO Heterojunction Transistors Processed from Solution. *Advanced Materials* **29**, 1605837 (2017).
34. Boucherit, M. *et al.* Modulation of over 10^{14} cm^{-2} electrons in SrTiO₃/GdTiO₃ heterostructures. *Appl. Phys. Lett.* **104**, 182904 (2014).
35. Kajdos, A. P., Ouellette, D. G., Cain, T. A. & Stemmer, S. Two-dimensional electron gas in a modulation-doped SrTiO₃/Sr(Ti, Zr)O₃ heterostructure. *Appl. Phys. Lett.* **103**, 082120 (2013).
36. Krusin-Elbaum, L. & Wittmer, M. Conducting Transition Metal Oxides: Possibilities for RuO₂ in VLSI Metallization. *J. Electrochem. Soc.* **135**, 2610 (1988).
37. Occhialini, C. A. *et al.* Local electronic structure of rutile RuO₂. *Phys. Rev. Res.* **3**, 033214 (2021).
38. Lu, Q. *et al.* Metal–insulator transition tuned by oxygen vacancy migration across TiO₂/VO₂ interface. *Sci Rep* **10**, 18554 (2020).
39. Passarello, D., Altendorf, S. G., Jeong, J., Samant, M. G. & Parkin, S. S. P. Metallization of Epitaxial VO₂ Films by Ionic Liquid Gating through Initially Insulating TiO₂ Layers. *Nano Lett.* **16**, 5475–5481 (2016).
40. Gunkel, F., Christensen, D. V., Chen, Y. Z. & Pryds, N. Oxygen vacancies: The (in)visible friend of oxide electronics. *Appl. Phys. Lett.* **116**, 120505 (2020).
41. Kalinin, S. V. & Spaldin, N. A. Functional Ion Defects in Transition Metal Oxides. *Science* **341**, 858–859 (2013).
42. Giampietri, A., Drera, G. & Sangaletti, L. Band Alignment at Heteroepitaxial Perovskite Oxide Interfaces. Experiments, Methods, and Perspectives. *Advanced Materials Interfaces* **4**, 1700144 (2017).

43. Schwab, C., Schraknepper, H. & De Souza, R. A. Oxygen transport in single-crystal LaAlO_3 substrates. *Phys. Rev. Mater.* **5**, 105001 (2021).
44. Scanlon, D. O. *et al.* Band alignment of rutile and anatase TiO_2 . *Nature Mater* **12**, 798–801 (2013).
45. Shibuya, K., Kawasaki, M. & Tokura, Y. Metal-insulator transitions in TiO_2/VO_2 superlattices. *Phys. Rev. B* **82**, 205118 (2010).
46. Aetukuri, N. P. Ph.D. thesis (Stanford University, 2013).
47. Kalha, C. *et al.* Hard x-ray photoelectron spectroscopy: a snapshot of the state-of-the-art in 2020. *J. Phys.: Condens. Matter* **33**, 233001 (2021).
48. Paez, G. J. *et al.* Simultaneous Structural and Electronic Transitions in Epitaxial $\text{VO}_2/\text{TiO}_2(001)$. *Phys. Rev. Lett.* **124**, 196402 (2020).
49. Quackenbush, N. F. *et al.* X-Ray Spectroscopy of Ultra-Thin Oxide/Oxide Heteroepitaxial Films: A Case Study of Single-Nanometer VO_2/TiO_2 . *Materials* **8**, 5452–5466 (2015).
50. Eguchi, R. *et al.* Photoemission evidence for a Mott-Hubbard metal-insulator transition in VO_2 . *Phys. Rev. B* **78**, 075115 (2008).
51. Gatti, M., Panaccione, G. & Reining, L. Effects of Low-Energy Excitations on Spectral Properties at Higher Binding Energy: The Metal-Insulator Transition of VO_2 . *Phys. Rev. Lett.* **114**, 116402 (2015).
52. Fratino, L., Bag, S., Camjayi, A., Civelli, M. & Rozenberg, M. Doping-driven resistive collapse of the Mott insulator in a minimal model for VO_2 . *Phys. Rev. B* **105**, 125140 (2022).
53. Solomon, P. M. & Morkoc, H. Modulation-doped GaAs/AlGaAs heterojunction field-effect transistors (MODFET's), ultrahigh-speed device for supercomputers. *IEEE Transactions on Electron Devices* **31**, 1015–1027 (1984).
54. Newns, D. M. *et al.* Mott transition field effect transistor. *Appl. Phys. Lett.* **73**, 780–782 (1998).
55. Yang, B.-J. & Nagaosa, N. Emergent Topological Phenomena in Thin Films of Pyrochlore Iridates. *Phys. Rev. Lett.* **112**, 246402 (2014).
56. Mondal, D. *et al.* Atomically-smooth single-crystalline VO_2 (101) thin films with sharp metal-insulator transition. *Journal of Applied Physics* **126**, 215302 (2019).
57. Schlueter, C. *et al.* The new dedicated HAXPES beamline P22 at PETRAIII. *AIP Conference Proceedings* **2054**, 040010 (2019).

Supplementary Information

Modulation-Doping a Correlated Electron Insulator

Debasish Mondal¹, Smruti Rekha Mahapatra¹, Abigail M Derrico², Rajeev Kumar Rai³, Jay R Paudel², Christoph Schlueter⁴, Andrei Gloskovskii⁴, Rajdeep Banerjee¹, Frank M F DeGroot⁵, Dipankar D Sarma¹, Awadhesh Narayan¹, Pavan Nukala³, Alexander X Gray^{2*} and Naga Phani B Aetukuri^{1*}

Affiliations:

1. Solid State and Structural Chemistry Unit, Indian Institute of Science, Bengaluru, Karnataka, 560012, India
2. Department of Physics, Temple University, 1925 N. 12th St., Philadelphia, PA 19122, USA
3. Centre for Nano Science and Engineering, Indian Institute of Science, Bangalore, Karnataka, 560012, India
4. Deutsches Elektronen-Synchrotron, DESY, 22607 Hamburg, Germany
5. Utrecht University, Inorganic Chemistry and Catalysis Group Universiteitsweg 99, 3584 CA Utrecht, The Netherlands

*Corresponding authors emails: phani@iisc.ac.in (N.B.A); axgray@temple.edu (A.X.G)

Table of Contents:

S1: Reflection High Energy Electron Diffraction (RHEED) of VO₂ thin films..... 3

S2: AFM images of VO₂ thin film and heterostructure 3

S3: Thomas-Fermi screening length calculation for VO₂ heterostructure..... 4

S4: A comparison of X-ray diffractograms for VO₂ thin films and heterostructures 5

S5: Reciprocal space maps (RSM) of VO₂ thin film and heterostructures..... 6

S6: Temperature-dependent sheet resistance of VO₂ thin films 7

S7: Temperature-dependent sheet resistance of VO₂ thin film and heterostructures 8

S8: Calculation of T_{MIT} from sheet resistance vs temperature curves 9

S9: Temperature-dependent sheet resistance of VO₂ heterostructures and controls 10

S10: Carrier density and carrier mobility for 7.5 nm VO₂ thin films and heterostructures 11

S11: Binding energy calibration of VO₂ spectra across the MIT 12

S12: Summary of Binding energy changes for modulation-doped VO₂..... 13

S13: Evolution of *PI* peak in metallic and insulating VO₂ heterostructures 14

S14: HAXPES spectra of V *2p*_{3/2}..... 15

S15: HAXPES spectra of La *3d* and Al *1s* 16

S16: Valence band spectra in insulating state for VO₂ heterostructures and thin films 17

S1: Reflection High Energy Electron Diffraction (RHEED) of VO₂ thin films

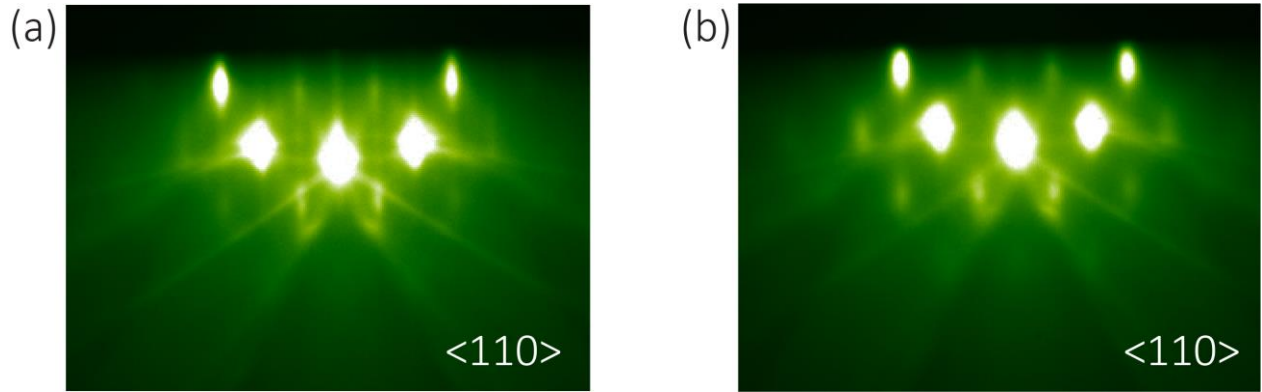


Fig. S1. RHEED pattern of VO₂ thin films on TiO₂ (001) substrate along the <110> direction for two different thicknesses of (a) 1.5 nm and (b) 9.5 nm. These patterns were captured at 425 °C just after the VO₂ deposition. RHEED patterns are indicative of single-crystalline VO₂ films with smooth film surfaces.

S2: AFM images of VO₂ thin film and heterostructure

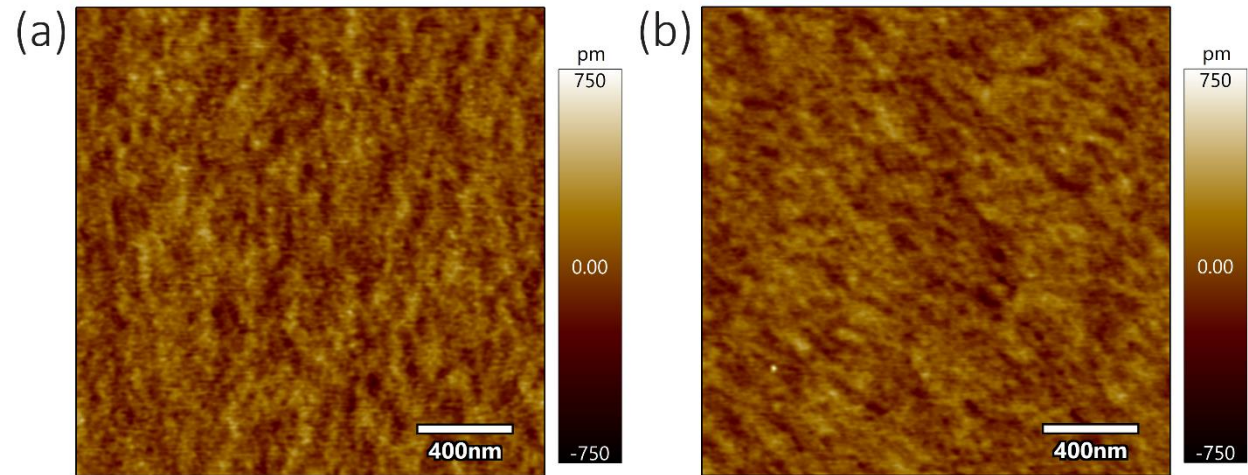


Fig. S2. AFM images of (a) 9.5 nm VO₂ film and (b) 9.5 nm VO₂ heterostructure on TiO₂ (001) substrate show smooth 2D surfaces with a root mean-square roughness in the range of 80-100 pm. The images were taken in the tapping mode (AC air topography) using an Asylum Cypher ES AFM.

S3: Thomas-Fermi screening length calculation for VO₂ heterostructures

Thomas-Fermi screening length (L) can be calculated as follows

$$L = \sqrt{\frac{K\varepsilon_0 T k_B}{e^2 n_e}}$$

where critical carrier density, $n_e \approx \left(\frac{0.25}{a_B}\right)^3$ and $K, \varepsilon_0, k_B, T, e, a_B$ are the dielectric constant (≈ 36)^{1,2} of VO₂, free space permittivity ($\approx 8.854 \times 10^{-12}$ F/m), Boltzmann constant ($\approx 1.380 \times 10^{-23}$ m² kg s⁻² K⁻¹), temperature of VO₂, electronic charge ($\approx 1.602 \times 10^{-19}$ C) and effective Bohr radius respectively. Effective Bohr radius (a_B) can be calculated as follows

$$a_B = \frac{h^2 K \varepsilon_0}{\pi m^* e^2}$$

where h is the Planck's constant ($\approx 6.626 \times 10^{-34}$ m²kg/s) effective mass of electron in VO₂, $m^* \approx 3.5m_e$.^{2,3} By plugging these above values and keeping $T \approx 300$ K, calculated Thomas-Fermi screening length (L) is ~ 0.73 nm.

S4: A comparison of X-ray diffractograms for VO₂ thin films and heterostructures

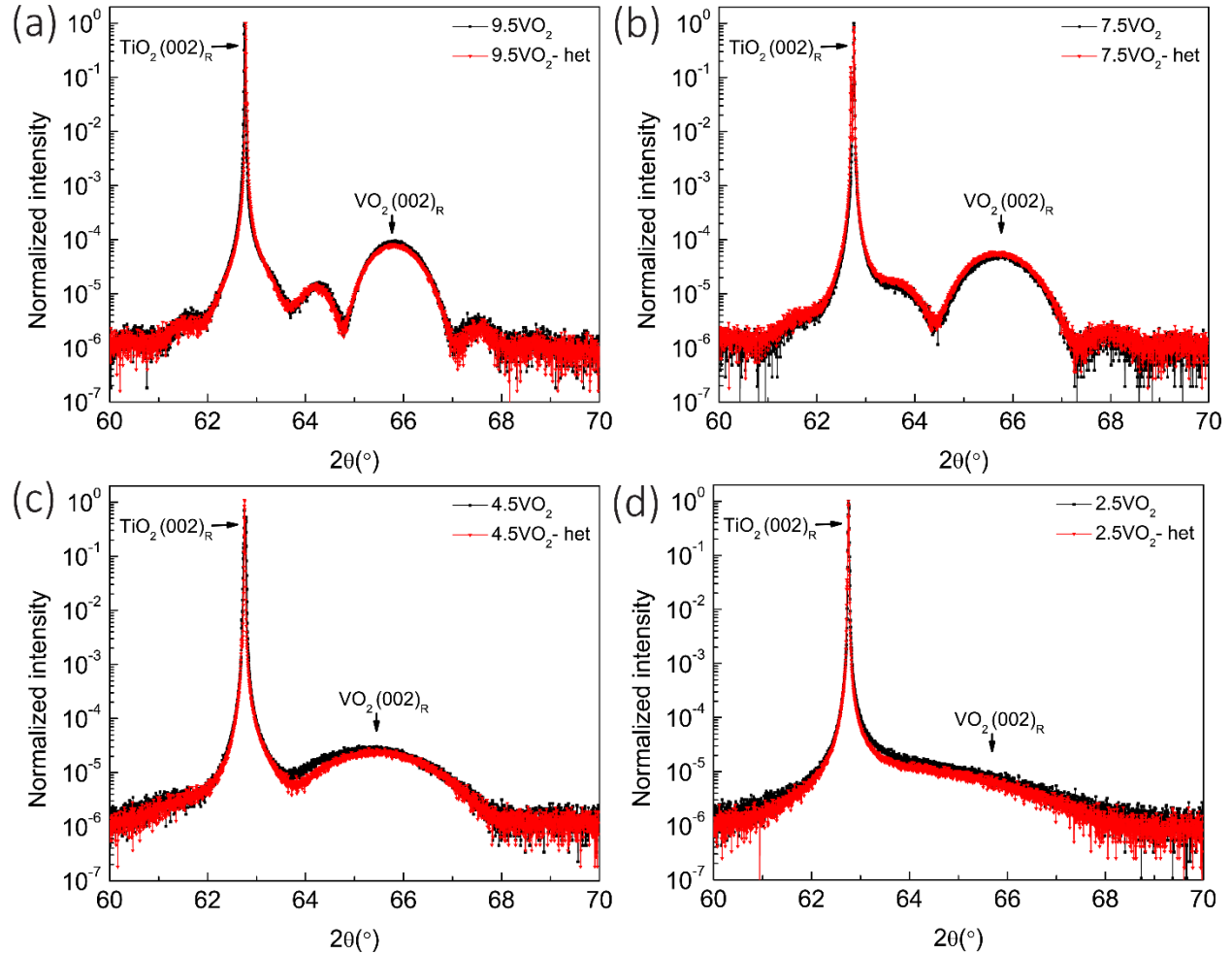


Fig. S4. Comparison of high-resolution θ - 2θ X-ray diffractograms of VO₂ (001) thin films (black) and heterostructures (red) at different VO₂ thicknesses of (a) 9.5 nm, (b) 7.5 nm, (c) 4.5 nm and (d) 2.5 nm. We showed in Fig. 2a of the main manuscript that there is no measurable change in the VO₂ lattice parameter, C_R , between VO₂ thin films and heterostructures. To further confirm this, we performed and compared high-resolution X-ray diffractograms for thin films and heterostructures with identical VO₂ thickness. Clearly, there is excellent overlap of the two diffractograms, including thickness fringes, for all thicknesses measured. This is clear indication that depositing heterostructures on ultra-thin VO₂ films did not affect the lattice parameters of VO₂.

S5: Reciprocal space maps (RSM) of VO₂ thin film and heterostructures

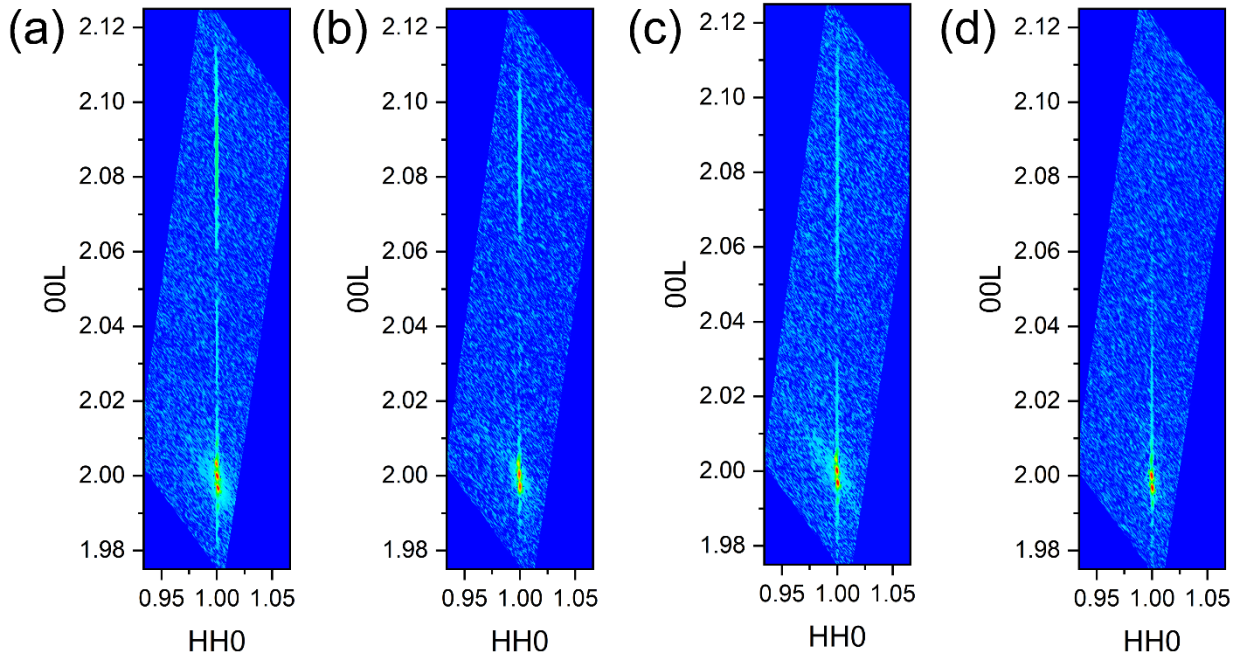


Fig. S5. Asymmetrical RSM images around (112) plane for (a) 9.5 nm VO₂ thin film, and VO₂ heterostructures with VO₂ thicknesses of (b) 9.5 nm (c) 6.5 nm and (d) 1.5 nm. The vertical and horizontal axis of all the plots is scaled relative to the miller indices of the TiO₂ (001) substrate. The RSM data presented here is further evidence that there are no measurable changes to the unit cell volume across all heterostructures and that all films are coherently strained to the TiO₂ (001) substrate.

S6: Temperature-dependent sheet resistance of VO₂ thin films

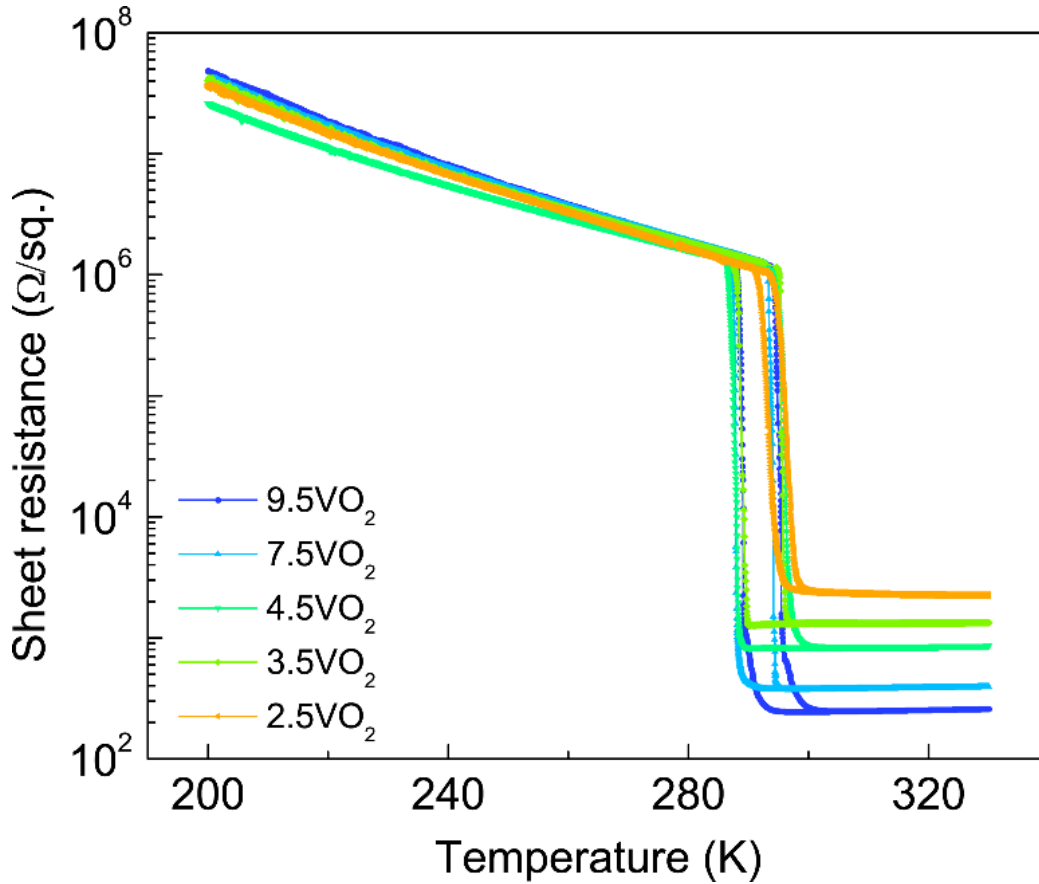


Fig. S6. Temperature-dependent sheet resistance of VO₂ thin films with varying VO₂ thicknesses as mentioned in the legends. For nomenclature simplicity, VO₂ thin films are written as $t\text{VO}_2$ where 't' is the thickness of VO₂. For example, 9.5VO₂ corresponds to a 9.5 nm thick VO₂ thin film. The increase in metallic state resistance as the thickness of VO₂ film is decreased is suggestive of interfacial scattering. This also shows all the films, except 2.5VO₂, have nearly the same transition temperature (~295 K) which again confirms the reduction in transition temperature in VO₂ heterostructures is entirely after the formation of the heterostructure. The slight increase in transition temperature for the 2.5VO₂ film is attributed to be due to titanium interdiffusion at the VO₂/TiO₂(substrate) interface.^{4,5} We were not able to measure 1.5 nm VO₂ thin film as it was found to be not stable when exposed to ambient without a capping layer.

S7: Temperature-dependent sheet resistance of VO₂ thin film and heterostructures

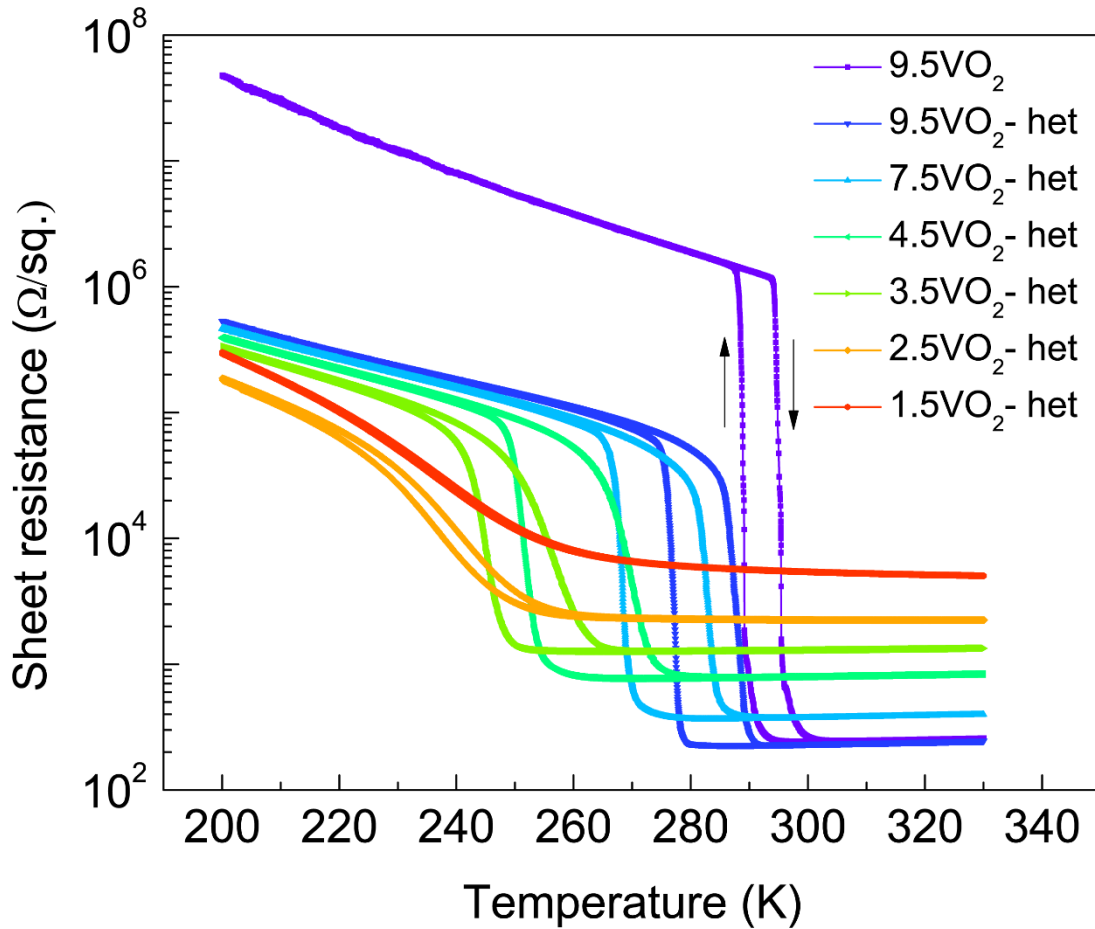


Fig. S7. Temperature-dependent sheet resistance of 9.5 nm VO₂ thin film and VO₂ heterostructures with varying VO₂ thicknesses, t . For nomenclature simplicity, we distinguish VO₂ thin films and heterostructures with a VO₂ thickness of ‘ t ’ as $t\text{VO}_2$ and $t\text{VO}_2\text{-het}$, respectively. For example, 9.5VO₂-het corresponds to a heterostructure with 9.5 nm thick VO₂. The sheet resistance data in this figure corresponds to the normalized resistance presented in Fig. 2b of the main text. The increase in metallic state resistance as the thickness of VO₂ film is decreased is suggestive of interfacial scattering. Importantly, it can be seen that the metallic state resistance is identical for the 9.5 nm VO₂ heterostructure and 9.5 nm VO₂ thin film. This is also an indirect indication of the sharp interfaces across the heterostructure layers; Rough interfaces could lead to increased interfacial scattering and a higher metallic state resistance for the 9.5 nm VO₂ heterostructure in comparison with the 9.5 nm VO₂ thin film.

S8: Calculation of T_{MIT} from sheet resistance vs temperature curves

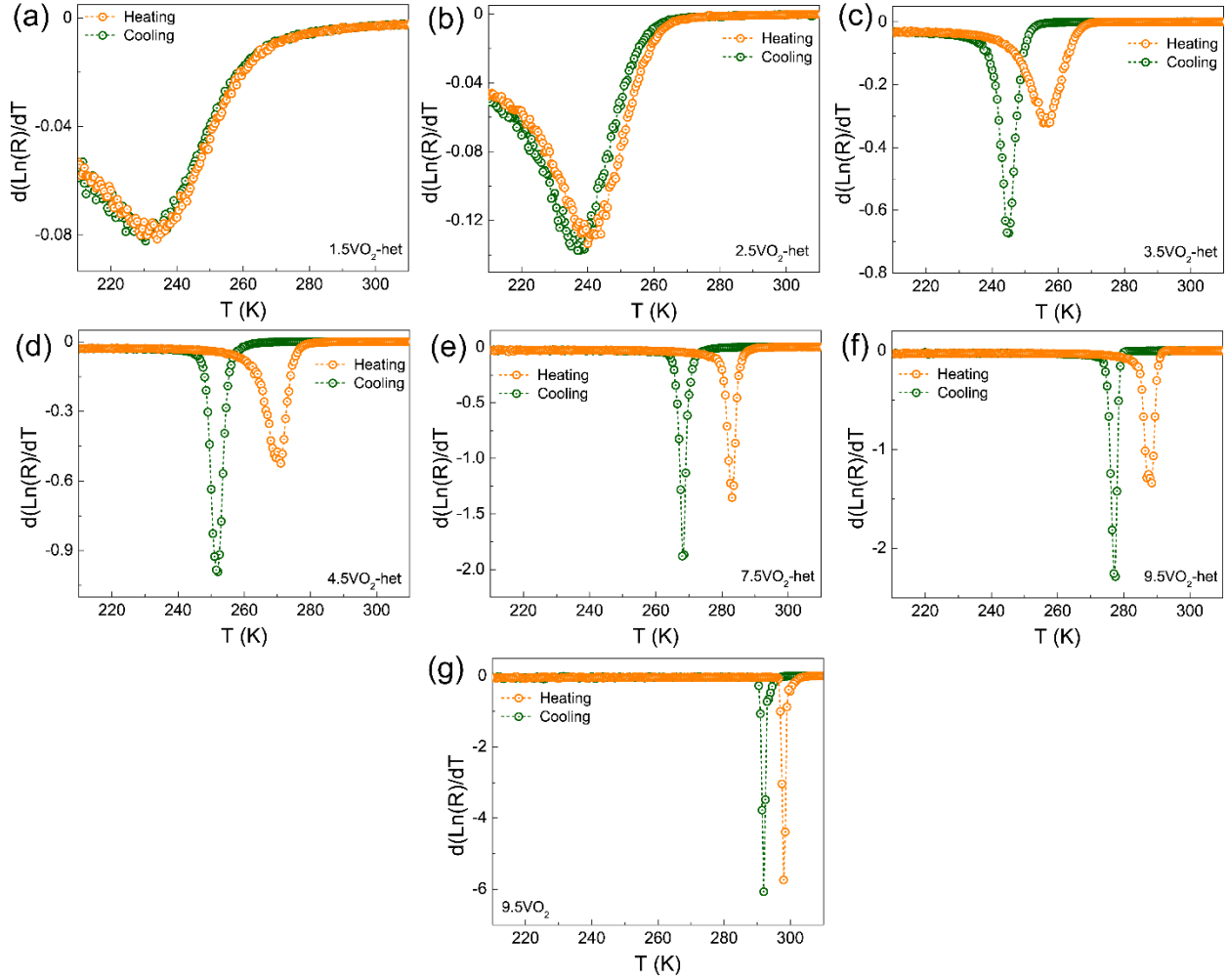


Fig. S8. $d(\ln(R))/dT$ plots for both the heating and cooling cycles for VO_2 heterostructures with VO_2 thicknesses of (a) 1.5 nm, (b) 2.5 nm, (c) 3.5 nm, (d) 4.5 nm, (e) 7.5 nm, (f) 9.5 nm, and, (g) for a 9.5 nm VO_2 thin film. Here, $\ln(R)$ is the natural log of the temperature-dependent sheet resistance of the films as shown in Fig. S7 and d/dT is the derivative operator with respect to temperature, T . Peak positions of the $d(\ln(R))/dT$ plots correspond to the transition temperature for the respective thermal cycle. All the transition temperatures discussed in the main text are the average transition temperature of the transition temperature for heating and cooling cycle given by $T_{MIT} = ((T_{MIT})_{heating} + (T_{MIT})_{cooling})/2$. The estimated T_{MIT} are: 233 K for 1.5 nm VO_2 ; 237 K for 2.5 nm VO_2 ; 250 K for 3.5 nm VO_2 ; 260 K for 4.5 nm VO_2 ; 275 K for 7.5 nm VO_2 ; 282 K for 9.5 nm VO_2 in VO_2 heterostructures. By comparison, the T_{MIT} is 295 K for 9.5 nm VO_2 thin film.

S9: Temperature-dependent sheet resistance of VO₂ heterostructures and controls

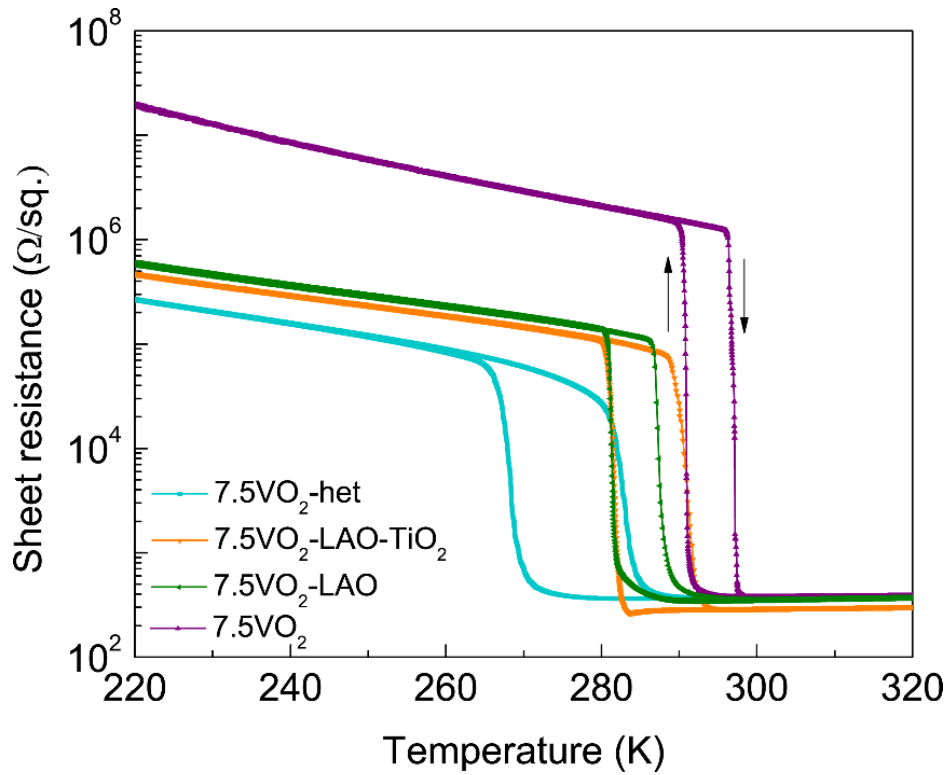


Fig. S9. A comparison of temperature-dependent sheet resistance characteristics of modulation-doped 7.5 nm VO₂ heterostructure (7.5VO₂-het) and 7.5 nm VO₂ thin film (7.5VO₂) with various VO₂ heterostructure ‘controls’. The control heterostructures include 7.5 nm VO₂ thin film capped with 2 nm LAO (7.5VO₂-LAO) and a 7.5 nm VO₂ heterostructure with a near stoichiometric TiO₂ deposited at 10 mTorr of oxygen pressure with a 1 nm LAO capping layer over TiO₂ (7.5VO₂-LAO-TiO₂). The number prefixed with each of the layers represent the respective film thickness in nm. For the 7.5VO₂-LAO heterostructure, there is a reduction in resistivity in the insulating phase and a small but observable reduction in transition temperature (T_{MIT}) ~6 K compared to the T_{MIT} of VO₂ thin film. However, for the modulation-doped heterostructure, (7.5VO₂-het), there is a further reduction in resistivity with a decrease in T_{MIT} of ~20 K compared to the T_{MIT} of VO₂ thin film. For the heterostructure where TiO₂ is near stoichiometric (7.5VO₂-LAO-TiO₂), the reduction in T_{MIT} is also ~6 K, similar to the reduction in T_{MIT} for 7.5VO₂-LAO. Clearly, a majority of the reduction in T_{MIT} comes from the charge transfer from the TiO_{2-x} dopant layer.

S10: Carrier density and carrier mobility for 7.5 nm VO₂ thin films and heterostructures

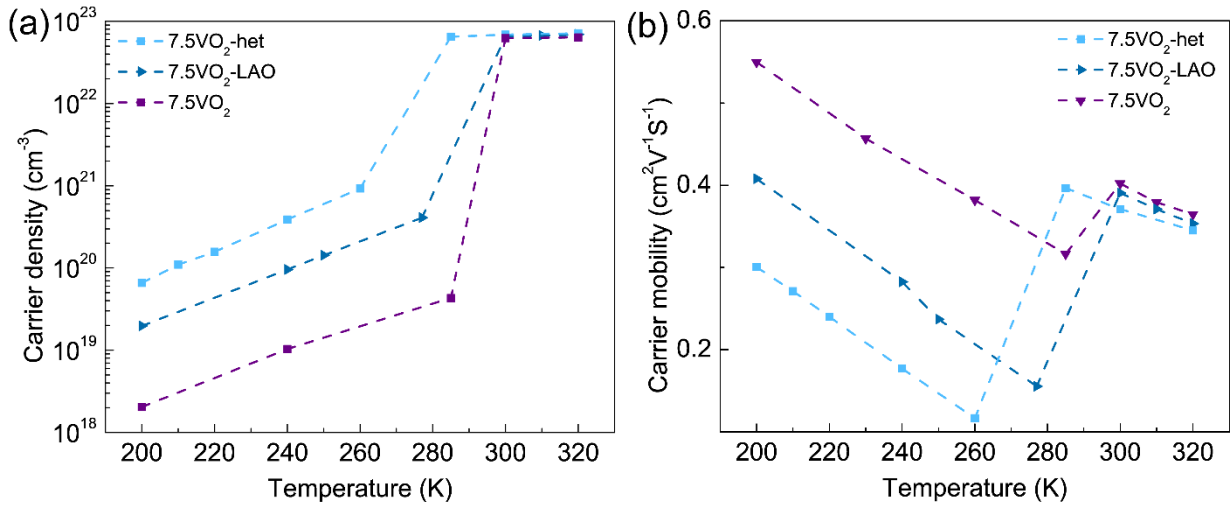


Fig. S10. Plots of temperature-dependent (a) carrier densities and (b) carrier mobilities for 7.5 nm VO₂ heterostructure (7.5VO₂-het), 7.5 nm VO₂ thin film (7.5VO₂) and 7.5 nm VO₂ capped with 2 nm LAO (7.5VO₂-LAO). For the 7.5VO₂-LAO, there is a noticeable increase in carrier density (and a decreased in carrier mobility) compared to 7.5 nm VO₂ thin film, but this is less than the carrier density observed in the comparable modulation-doped heterostructure (7.5VO₂-het).

S11: Binding energy calibration of VO₂ spectra across the MIT

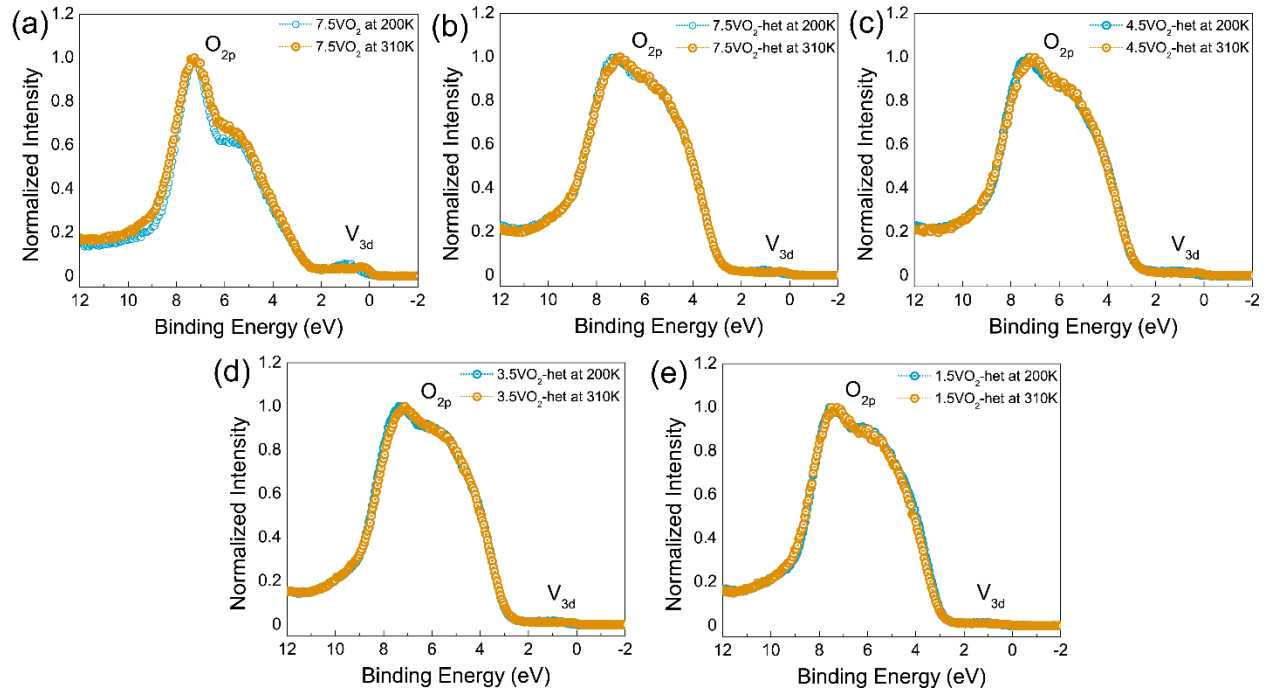


Fig. S11. Binding energy calibration for the insulating state spectra. We noticed charging effects in some of the insulating state HAXPES spectra. In order to correct for charging effects, we used O 2p binding energy across insulating and metallic states of the samples as an internal reference. We note that metallic state spectra are unaffected by charging effects and several previous studies showed that binding energy of O 2p spectra does not change across the MIT⁶⁻⁹. Further, no changes to the O 2p contributions from the LAO and TiO₂ layers are expected across the MIT in VO₂. The valence band spectra for (a) 7.5 nm VO₂ film and VO₂ heterostructures with VO₂ thicknesses of (b) 7.5 nm, (c) 4.5 nm, (d) 3.5 nm, and (e) 1.5 nm are shown for both the metallic phase (at 310 K) and the insulating phase (at 200 K) after binding energy correction. All the V 2p spectra shown in the main text are based on this calibration.

S12: Summary of Binding energy changes for modulation-doped VO₂

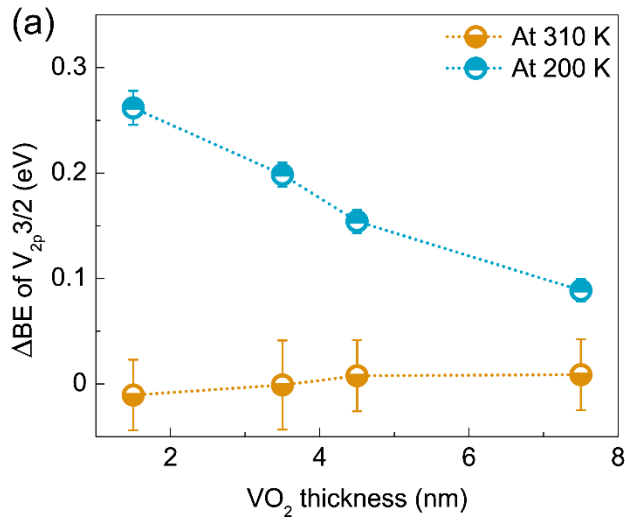


Fig. S12. The change in binding energy of the V $2p_{3/2}$ peak for VO₂ heterostructures with respect to its binding energy in VO₂ thin films (ΔBE) for various thicknesses of VO₂ in heterostructures. There is no binding energy change in the metallic state (orange, at 310 K), while there is a binding energy increase for the same set of samples in the insulating state (blue, at 200 K). This is suggestive of band-bending leading to modulation-doping.

S13: Evolution of $P1$ peak in metallic and insulating VO_2 heterostructures

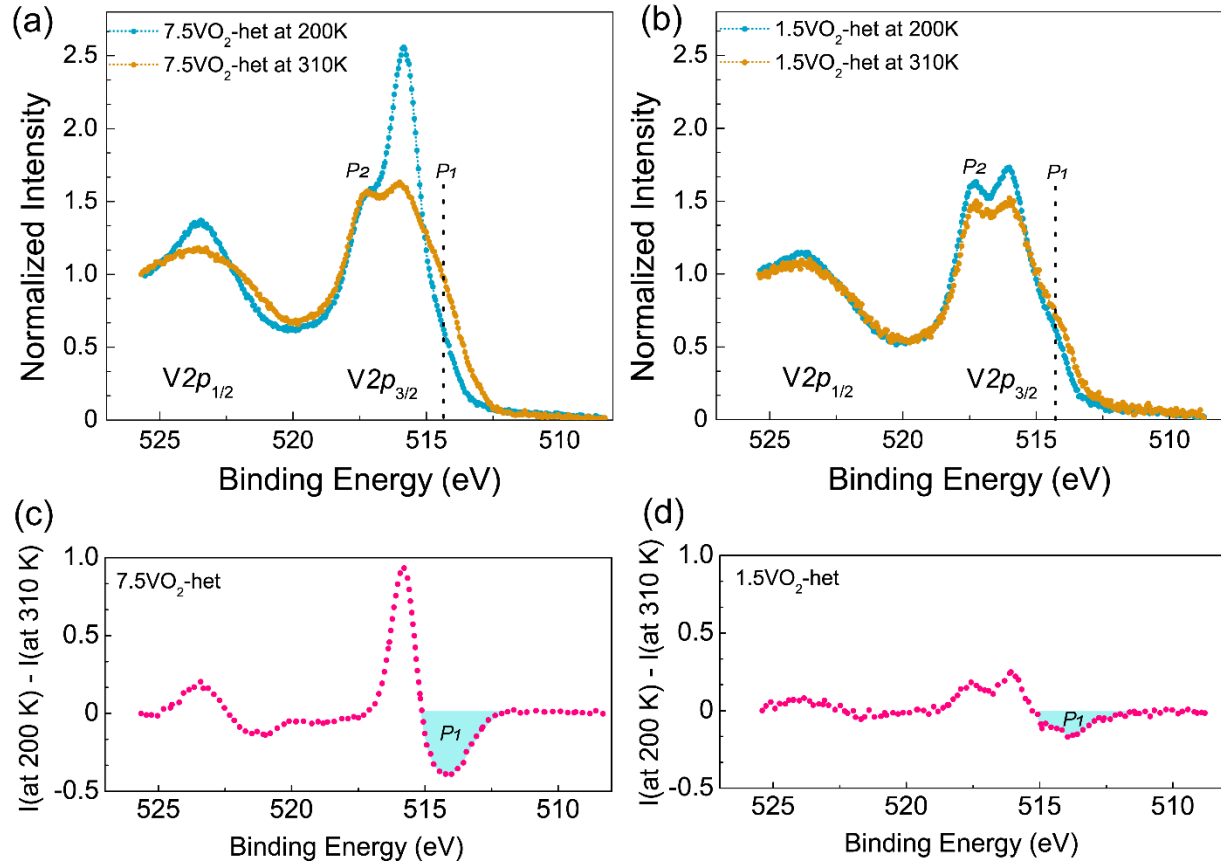


Fig. S13. $V 2p$ core level spectra for (a) 7.5 nm and (b) 1.5 nm VO_2 heterostructures in the metallic (at 310 K) and insulating (at 200K) states normalized to the $V 2p$ area under the curve. Corresponding intensity difference plots in (c) showing that the $P1$ peak (at ~ 514.5 eV) is prominent in the metallic phase for the 7.5 nm VO_2 heterostructure (negative intensity difference) while for the 1.5 nm heterostructure in (d) the intensity difference decreases suggesting an increase in the $P1$ intensity for the insulating state spectrum for the 1.5 nm VO_2 heterostructure.

S14: HAXPES spectra of V $2p_{3/2}$

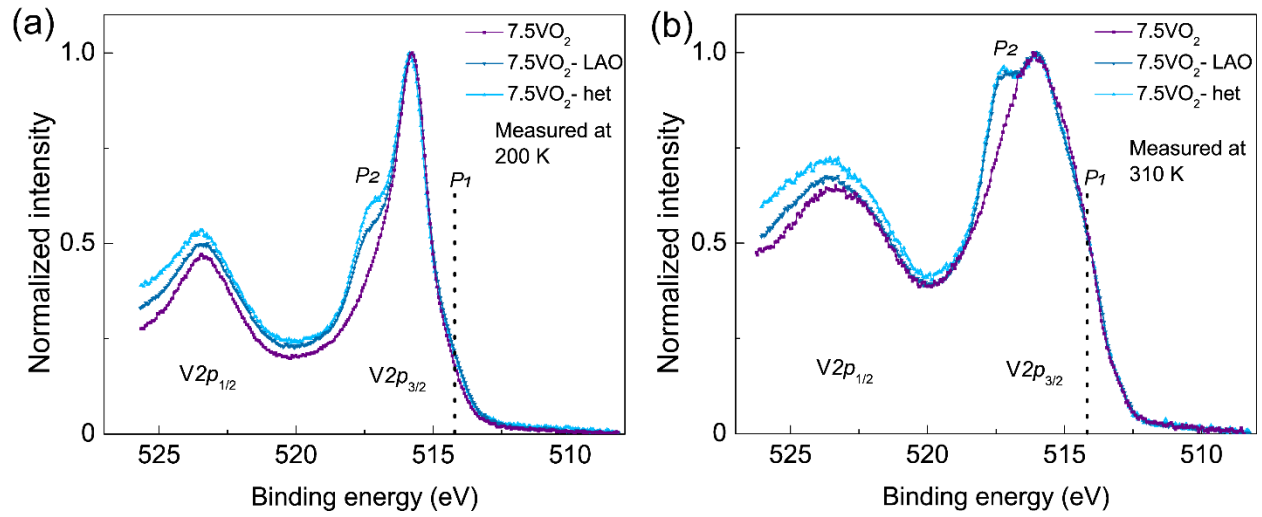


Fig. S14. A comparison of V $2p$ core-level spectra of 7.5 nm modulation doped VO₂ heterostructure, 7.5 nm VO₂ with 2 nm LAO capping layer and 7.5 nm VO₂ thin film in (a) the insulating (200 K) and (b) the metallic states (310 K). The additional peak P₂ is observed after the deposition of LAO. However, the change in the peak P₁ in the insulating state spectra is not significant.

S15: HAXPES spectra of La 3d and Al 1s

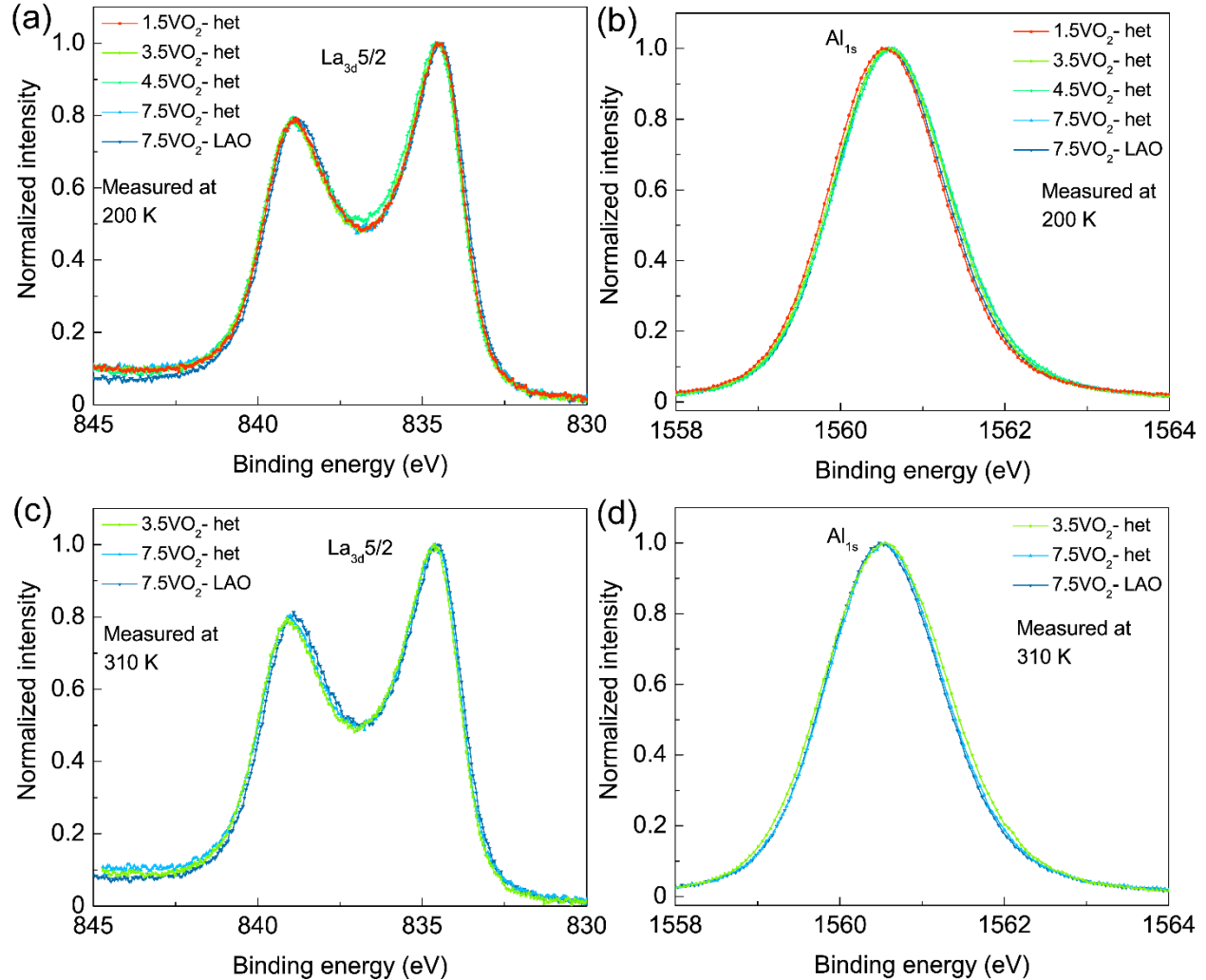


Fig. S15. A comparison of core level HAXPES spectra of modulation doped VO₂ heterostructures of (a) La 3d_{5/2} and (b) Al 1s at 200 K, and (c) La 3d_{5/2} (d) Al 1s at 310 K. In the insulating state (at 200 K), the spectra were collected for VO₂ heterostructures corresponding to all VO₂ thicknesses used in this study. In the metallic state (at 310 K), the spectra were collected for 3.5 nm and 7.5 nm VO₂ heterostructures and for 7.5VO₂/2LAO heterostructure. No significant changes to the La and Al core level were observed.

S16: Valence band spectra in insulating state for VO₂ heterostructures and thin films

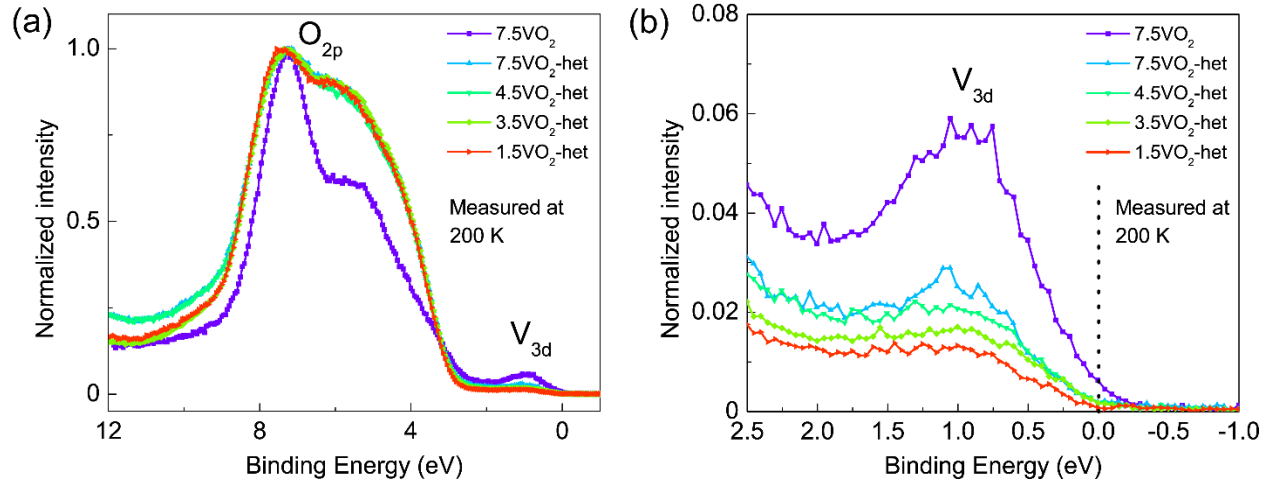


Fig. S16. (a) Valence band spectra (*O* 2*p* and *V* 3*d*) and, (b) *V* 3*d* spectra (zoom in of figure S16 a) measured at 200 K are shown here after the binding energy correction as discussed in S11. The *V* 3*d* peak position at ~ 0.9 eV is in good agreement with existing literature.^{6–9} The vertical dotted line at 0 eV corresponds to the Fermi level.

Supplementary References

1. Yang, Z., Ko, C., Balakrishnan, V., Gopalakrishnan, G. & Ramanathan, S. Dielectric and carrier transport properties of vanadium dioxide thin films across the phase transition utilizing gated capacitor devices. *Phys. Rev. B* **82**, 205101 (2010).
2. Paik, H. *et al.* Transport properties of ultra-thin VO₂ films on (001) TiO₂ grown by reactive molecular-beam epitaxy. *Appl. Phys. Lett.* **107**, 163101 (2015).
3. Rosevear, W. H. & Paul, W. Hall Effect in VO₂ near the Semiconductor-to-Metal Transition. *Phys. Rev. B* **7**, 2109–2111 (1973).
4. Martens, K., Aetukuri, N., Jeong, J., Samant, M. G. & Parkin, S. S. P. Improved metal-insulator-transition characteristics of ultrathin VO₂ epitaxial films by optimized surface preparation of rutile TiO₂ substrates. *Appl. Phys. Lett.* **104**, 081918 (2014).
5. Mondal, D. *et al.* Atomically-smooth single-crystalline VO₂ (101) thin films with sharp metal-insulator transition. *Journal of Applied Physics* **126**, 215302 (2019).

6. Taguchi, M., Takata, Y. & Chainani, A. Hard X-ray photoelectron spectroscopy: A few recent applications. *Journal of Electron Spectroscopy and Related Phenomena* **190**, 242–248 (2013).
7. Quackenbush, N. F. *et al.* X-Ray Spectroscopy of Ultra-Thin Oxide/Oxide Heteroepitaxial Films: A Case Study of Single-Nanometer VO₂/TiO₂. *Materials* **8**, 5452–5466 (2015).
8. Quackenbush, N. F. *et al.* Nature of the Metal Insulator Transition in Ultrathin Epitaxial Vanadium Dioxide. *Nano Lett.* **13**, 4857–4861 (2013).
9. Eguchi, R. *et al.* Electronic structure of 3d¹ configuration vanadium oxides studied by soft X-ray and hard X-ray photoemission spectroscopy. *Journal of Electron Spectroscopy and Related Phenomena* **156–158**, 421–425 (2007).